UNIVERSITY OF JYVÄSKYLÄ

Fabrication of Free-Standing Piezoelectric Nanostructures for Thermal Transport Studies

Master's Thesis

Tero J. Isotalo

Department of Physics

May 21, 2007

LaTeX 2_ε

Acknowledgments

This thesis work was completed at the University of Jyväskylä in Finland with experimental research carried out at the facilities of the Nanoscience Center. First and foremost, I would like to thank professor Ilari Maasilta for the opportunity to work on this challenging project and for his direction and encouragement throughout. Additionally, I would like to extend my gratitude to Panu Koppinen for his assistance and expertise. Thanks also to Jenni Karvonen, Jussi Toppari, and Andreas Johansson for their advice especially in fabrication. I would like to give special mention to Antti Nuottajärvi and Tarmo Suppula for their invaluable contributions in addressing technical issues during this project. And of course, none of this would have been possible without the encouragement and support of my father, Heikki. Kiitän myös sukulaisiani suomessa keiden tuki, varsinkin muutossa ja suhtautumisessa, on ollut korvaamatonta.

Contents

List of Figures

Abstract

Free-standing nanostructures for thermal transport studies have been fabricated from piezoelectric AlN thin films deposited on a Si substrate. The piezoelectric AlN was deposited using reactive sputtering by collaborators at the University of Uppsala. Thermal transport measurements, performed by SINIS thermometry, required integration of the tunnel junction process with that of the free-standing nanostructure fabrication. Several processing challenges have been dealt with and the fabrication recipe is discussed in detail.

Introduction

As the fabrication of nanoscale devices has seen a great increase in the past years, the study of their electronic and optical properties has similarly increased. Thermal properties however, have received notably less attention. The performance of ultra-sensitive, low-temperature radiation detectors, for example, is limited by thermal coupling to the substrate in the form of phonon noise. It is therefore important in the manufacturing of such devices that the thermal properties are well understood. In order to measure thermal transport properties in nanostructures, one needs to isolate them from a number of environmental sources of noise.

The goal of this research project is to measure the effects of the piezoelectric field on thermal transport. Specifically, we hope to observe the coupling of thermal phonon modes through a vacuum. The electromechanical coupling of the piezoelectric field is expected to allow transport of phonon modes across the vacuum gap between the emitting and receiving structures. Given a small enough gap, the piezo-field of the emitting side should extend across the vacuum, couple electromechanically, and induce corresponding phonon modes in the receiving side. These received phonon modes will then be measured as a thermal signature in the SINIS structure. The focus of this paper is on the fabrication of a device to investigate piezoelectric phenomena as they relate to thermal transport. Section 1

covers some theoretical background as well as principles of equipment used. Fabrication of samples is described in Section 2 while measurement procedure and results are discussed in Section 3. Analysis of results are discussed in Conclusions.

1 Background

1.1 SINIS Thermometer

While tunneling is a familiar quantum mechanical phenomenon, the properties of superconductors make their use in tunnel junctions of particular interest and utility. In 1960, Ivar Giaever observed electron tunneling in a Normal metal-Insulator-Superconductor (NIS) junction. Subsequent experiments with such tunnel junctions verified the BCS theory of superconductivity and in 1973, Giaever shared the Nobel prize in physics with Brian Josephson and Leo Esaki. Since then, the technology of NIS junctions has changed relatively little.

1.1.1 Tunneling

The tunnel barrier is commonly approximated by a rectangular potential between two conducting materials. In the case of a normal metal-insulator-superconductor junction, the tunneling behavior can be visualized as shown in Figure 1.1 below.

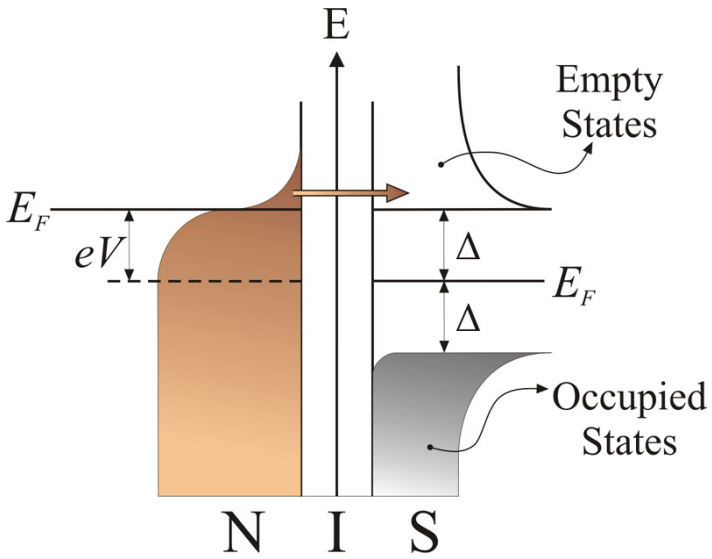

Figure 1.1: An energy diagram for a NIS junction shows "hot" electrons in the Fermi tail of the normal metal excited to energies just above the superconducting gap, allowing them to tunnel through the insulator into the unoccupied states in the superconductor.

When a voltage lower than Δ/e is applied over the junction, the electrons in the tail of the Fermi distribution of the normal metal just reach the top of the superconducting energy gap. Due to the forbidden zone of electron states in this gap, no tunneling current occurs. At voltages above Δ/e, these "hot" electrons are excited above the gap and are then able to tunnel through the insulator into the superconductor, resulting in a current through the junction.

1.1.2 NIS Junctions

The SINIS structure consists of two symmetric NIS junctions and as such, can be understood by inspecting the behavior of a single NIS junction. The I-V characteristics of a NIS junction are similar to those of a diode [1]. At voltages near the edge of the superconducting gap, there is a sharp increase in current which then assumes the familiar form of a resistor at significantly larger voltages. The density of states in the superconductor $N_s(E)$ is zero for quasi-electrons of energy E less than Δ. Above the gap, energy is given by [2]

$$N_S(E) = N_N(E)\frac{|E|}{\sqrt{E^2-\Delta^2}}\,, \tag{1.1}$$

where $N_N(E)$ is the density of states in the normal metal. Assuming the density of states in the normal metal to be constant near the Fermi energy, the tunneling current can be written [2, 3]

$$I(V) = \frac{1}{eR_T}\int_{\Delta}^{\infty}\frac{|E|}{\sqrt{E^2-\Delta^2}}[f(E-eV,T_e)-f(E+eV,T_e)]\mathrm{d}E\,, \tag{1.2}$$

where $R_T = [AeN_N(0)N_N(0)]^{-1}$, e is the electron charge, and T_e is the temperature of electrons in the normal metal. Here, the tunneling coefficient A contains the tunneling matrix elements $|T^{(i)}|$ and is given by [4]

$$A = \frac{4\pi e^2}{\hbar}|T^{(i)}|^2\,. \tag{1.3}$$

Note that the current in the NIS junction does not depend on the temperature of the superconductor, but is very sensitive to the temperature of the normal metal. By applying a current bias through the junction, one can measure the voltage V and use the characteristic Fermi distribution $f(E - eV, T_e)$ to calibrate the voltage-temperature dependence of the normal metal. A typical measured V-T curve is shown in Figure 1.2.

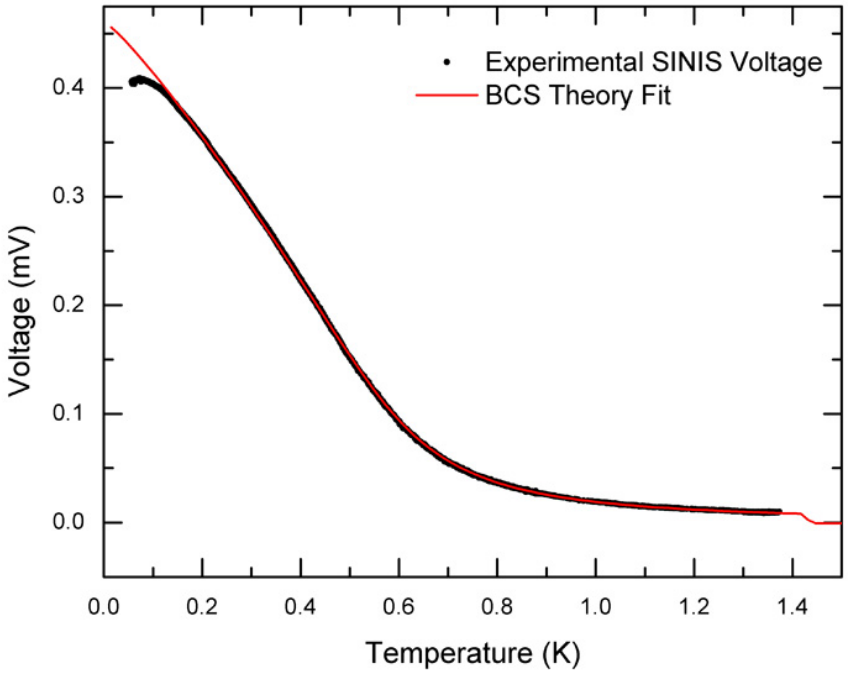

Figure 1.2: Voltage is measured across a SINIS structure at varying temperatures with a fixed current bias. The red curve is a fit of the BCS theory used in calibrating the SINIS.

The deviation of experimental data from BCS theory seen in Figure 1.2 at low temperatures is indicative of the noise inherent in the system. This is largely a consequence of the small size of the tunnel junctions (see Section 1.3.1). At $T_e = 0$, tunneling current will be zero for voltages below the superconducting gap as the density of states in the superconductor is zero in this region. Above Δ/e, the tunneling current can be approximated by

$$I(V) = \frac{\sqrt{V^2 - (\Delta/e)^2}}{R_T} \, . \tag{1.4}$$

As temperature T_e increases, the region in which the diode-like upturn in current takes place becomes more rounded. This limits the temperature range in which the SINIS thermometer is accurate to $\leq 0.4\ T_c$ [5] where T_c is the critical temperature of the superconductor. Also limiting the performance of a SINIS thermometer is the thermal relaxation time τ of the sensing element (normal metal) given by

$$\tau = \left(\frac{\partial \dot{Q}_{e-ph}}{\partial T_e} \right)^{-1} C_e \ , \tag{1.5}$$

where $\dot{Q}_{e-ph} = \Sigma\Omega(T_e^5 - T_{ph}^5)$ is the heat current between electrons and phonons for thick ($t >$30 nm) metal films [6] and $C_e = \Omega\gamma T_e$ is the electronic heat capacity, with γ being the so-called Sommerfeld constant [3]. Substituting the expressions for heat current and electronic heat capacity into (1.5), we arrive at the following:

$$\tau_{e-ph} = \frac{\gamma}{5\Sigma} T_e^{-3} \ . \tag{1.6}$$

Thus, we see that the response time of a SINIS thermometer is independent of the volume of the normal metal island. It depends on temperature and materially on the average electron-phonon scattering rate [3]. Such SINIS structures have been used successfully as sub-Kelvin thermometers and to directly measure the above mentioned electron-phonon relaxation rate in thin copper films [7].

1.2 Phonons

1.2.1 Insulators

The Debye theory is based on the assumption that lattice vibrations in a solid are caused by quantum oscillators [8]. These oscillators are characterized by and emit energy in quantized packets which can be considered to behave like particles. Much like the photon is an energy quantum of electromagnetic radiation, the phonon is an energy quantum of a lattice vibration. For insulators, phonons are the dominant source of thermal energy transfer and thus, energy transfer

is determined by lattice vibrational states. At high temperatures, all possible vibrational states of the atoms are excited.

A given phonon wavevector $\mathbf{q}$ in a crystal of volume V has a corresponding q-space volume $(2\pi)^3/V$ [9]. The number of modes N of each polarization whose wavevector is smaller than q is then

$$N = \frac{V}{(2\pi)^3}\left(\frac{4\pi q^3}{3}\right) , \tag{1.7}$$

where $(4\pi q^3/3)$ is the volume of a sphere of radius q. The dispersion relation is assumed to be linear and defined by $\omega = v_s q$, where v_s is the average acoustic velocity defined by

$$\frac{1}{v_s^3} = \frac{1}{3}\left(\frac{1}{v_\ell^3} + \frac{1}{v_{t1}^3} + \frac{1}{v_{t2}^3}\right) . \tag{1.8}$$

where v_ℓ, v_{t1}, and v_{t2} are the longitudinal and the two transverse acoustic velocities respectively. The density of states given by $D(\omega) = \mathrm{d}N/\mathrm{d}\omega$ can then be written

$$D_m(\omega) = \begin{cases} \dfrac{3V}{2\pi^2 v_s^3}\omega^2 & \text{for } \omega \le \omega_D \\ 0 & \text{for } \omega > \omega_D \end{cases} , \tag{1.9}$$

where the maximum ω_D is called the Debye frequency and is defined by

$$\omega_D^3 = 6\pi^2 v_s^3 \frac{N}{V} . \tag{1.10}$$

For a system of three-dimensional vibrational normal modes $\mathbf{q}m$ with occupation number $n_{\mathbf{q}m}$ and frequency $\omega_{\mathbf{q}m}$, the quantum mechanical Hamiltonian can be written

$$E_{tot} = \sum_{\mathbf{q}m}\left(n_{\mathbf{q}m} + \frac{1}{2}\right)\hbar\omega_{\mathbf{q}m} , \tag{1.11}$$

where $\mathbf{q}$ is the wave vector and m is the direction, or polarization, of the mode. In contrast to photons, which have two possible transverse polarizations, phonons have an additional degree of freedom allowing longitudinal polarization. Continuing with the assumption that phonons behave as a collection of identical harmonic oscillators [9], we can describe the thermally averaged occupation number by the Bose-Einstein function

$$\langle n_{\mathbf{q}m} \rangle = \frac{1}{e^{\hbar\omega_{\mathbf{q}m}/k_B T} - 1} \, . \tag{1.12}$$

The average energy of the mode $\mathbf{q}m$ at a temperature T is then

$$\langle E_{\mathbf{q}m} \rangle = \left(\langle n_{\mathbf{q}m} \rangle + \frac{1}{2} \right) \hbar\omega_{\mathbf{q}m} \, , \tag{1.13}$$

and the total energy will be given by summing the energies over all the phonon modes $\mathbf{q}$ and polarizations m as follows:

$$E_{tot} = \sum_{\mathbf{q}m} \left(\langle n_{\mathbf{q}m} \rangle + \frac{1}{2} \right) \hbar\omega_{\mathbf{q}m} = \sum_{\mathbf{q}m} \left(\frac{1}{e^{\hbar\omega_{\mathbf{q}m}/k_B T} - 1} + \frac{1}{2} \right) \hbar\omega_{\mathbf{q}m} \, . \tag{1.14}$$

In the equation above, it can be seen that the temperature-dependent contribution to total energy falls off exponentially. At low enough temperatures, this contribution vanishes leaving only the temperature-independent part or "zero-point" energy $\frac{1}{2}\hbar\omega$. This phenomenon is often referred to as the "freezing out" of higher temperature phonons.

1.2.2 Phonon Heat Capacity

Heat capacity at constant volume is defined

$$C_V = \left(\frac{\partial U}{\partial T} \right)_V \, . \tag{1.15}$$

When the temperature is such that $k_B T/\hbar < \omega_D$ but still much larger than the frequency difference between modes, the sum over $\mathbf{q}$ in (1.14) can be replaced with an integral [9, 10]. Assuming the number of modes at a given polarization m to be $D_m(\omega)$, the total energy, neglecting zero point energy, can then be approximated by

$$E = \sum_m \int D_m(\omega) \, \frac{\hbar\omega_m}{e^{\hbar\omega/k_B T} - 1} \, \mathrm{d}\omega \, . \tag{1.16}$$

Taking the derivative with respect to temperature T, we get the heat capacity for the lattice.

$$C_{\mathrm{lat}} = \left(\frac{\partial U}{\partial T}\right)_V = k_B \int D_p(\omega) \left(\frac{\hbar\omega}{k_B T}\right)^2 \frac{e^{\hbar\omega/k_B T}}{\left(e^{\hbar\omega/k_B T} - 1\right)^2} \, \mathrm{d}\omega \tag{1.17}$$

It should be noted here that there exists a lower limiting temperature for the integral approximation in (1.16) which depends on the solid dimensions. In a 1 mm^3 solid, the limit is 0.2 mK and in a 10 μm^3 solid it is as high as 20 mK [10]. This means that for nano-scale structures at very low temperatures, the approximation breaks down. The insulating solids in the preliminary measurements of this study are on the order of 0.03 mm^3 and thus fall well within the approximation boundaries. In the case of very thin suspended bridges however, this effect needs to be taken into account.

1.2.3 Thermal Resistivity

Scattering from crystal boundaries or impurities and phonon-phonon interactions determine the mean free path l of phonons and thus the thermal resistivity of the phonon gas. The Debye temperature θ_D defines important ranges for the phonon interactions and is defined by [9]

$$\theta_D = \frac{\hbar\nu}{k_B} \left(\frac{6\pi^2 N}{V}\right)^{1/3} \, . \tag{1.18}$$

Intermediate temperatures $T \leq \theta_D/10$ are dominated by phonon-phonon interactions [11]. Decreasing temperatures reduce the number of phonon modes and thus increases the phonon mean free path. Typical temperatures in this study are lower still and thus, a rigorous treatment is omitted here. A thorough discussion of thermal conductivity in this regime can be found in the literature [10]. At much lower temperatures $T \ll \theta_D$, the number of phonons is small enough that their effects on scattering can be neglected. Crystal boundaries and defects become the primary scattering agents. The dominant phonon wavelength at these temperatures is typically larger than the size of lattice impurities [11], thus further restricting the scattering to lattice boundaries.

1.2.4 Thermal Boundary Resistance

Thermalization between two materials at low temperatures becomes complicated due to the increasing importance of boundary resistance with decreasing temperature. In the case of an insulator in contact with liquid helium for example, energy is transfered only by phonons. This brings into consideration the acoustic mismatch between the two materials via Snell's law. The temperature difference at a boundary with heat $\dot{Q}$ flowing across it is given by [11]

$$\Delta T = R_K \dot{Q} \,, \tag{1.19}$$

where R_K is the Kapitza resistance. This boundary resistance is a function of the acoustic impedance of each material given by $Z = \rho v$, where ρ is the mass density of the material and v is the acoustic velocity for the mode in question. For small changes in temperature ($\Delta T \ll T$), the Kapitza resistance between two materials can be written

$$R_K = \frac{\Delta T}{\dot{Q}} = \frac{\mathrm{d}T}{\mathrm{d}\dot{Q}} = \frac{15\,\hbar^3 \rho_2 v_2^3}{2\pi^2\, k_B^4\, T^3 A \rho_1 v_1} \,, \tag{1.20}$$

where A is the contact area. It can be seen from the above equation that the Kapitza resistance is inversely proportional to the contact area and grows very

quickly with decreasing temperature.

1.3 Electron-Phonon Interactions

1.3.1 Metals

In addition to lattice vibrations, a metal also has conduction electrons which contribute to, and in fact dominate, thermal energy transfer. This dominance results from the Fermi velocity v_F being much greater than the sound velocity v_s of phonons [11]. These electrons are coupled to the phonons via electrostatic interactions as the lattice vibration results in a change in the charge density [10]. Calculating the strength of this interaction can be simplified by using the Born-Oppenheimer approximation. This makes use of the fact that electrons will react very quickly to movements by the comparatively massive ions. Modeling the electron-phonon interaction can be simplified using scalar deformation potential theory. This assumes that electrons scatter only from the deformation part of lattice vibrations and applies to ordered metal films [6], defined such that $ql > 1$, where q is the thermal phonon wavevector and l is the electron mean free path. For disordered films ($ql < 1$), electron scattering is affected strongly by impurities and boundaries, thus complicating the model. The complication arises from taking into account the interference between electron-phonon and electron-impurity interactions and a discussion can be found in the literature [6, 12].

Of particular interest is the weakened electron-phonon coupling in small volumes of metals at low temperature. In order to calculate the flow of power between electrons and phonons in a volume V, we take the energy lost by an electron in emitting a longitudinal phonon of wavevector q and multiply it by the rate of phonon emission $\Gamma_{\mathbf{q}-}$, whose exact form and derivation can be found in the literature [10]. Since the emission process involves phonons of all wavevectors $\mathbf{q}$, $P_e = \epsilon_q \Gamma_{\mathbf{q}-}$ should be summed over the range, taking into account the initial occupation probability $f(E_{\mathbf{k}})$ such that

$$P_e = 2\sum_{\mathbf{k}}\sum_{\mathbf{q}} \epsilon_q \, f(E_{\mathbf{k}})\Gamma_{\mathbf{q}-} \ , \tag{1.21}$$

with the factor of two appearing due to electron spin. Similarly, the total power of absorption is given by

$$P_a = 2\sum_{\mathbf{k}}\sum_{\mathbf{q}} \epsilon_q \, f(E_{\mathbf{k}})\Gamma_{\mathbf{q}+} \ . \tag{1.22}$$

The net power flow is given by $P = P_e - P_a$, which can be separated into power emitted at zero temperature P_0 and at finite temperature P_T. These powers can be expressed as [10]

$$\begin{aligned} P_0 &= \Sigma V T_{\text{el}}^5 \\ P_T &= \Sigma V T_{\text{ph}}^5 \ , \end{aligned} \tag{1.23}$$

where T_{el} and T_{ph} are the electron and phonon temperatures respectively. The coupling constant Σ is typically on the order of 0.1-1$\times 10^9$ W/m^{3}K^5 for metals [10]. Now, the net power flow out of the electrons can be written

$$P = \Sigma V (T_{\text{el}}^5 - T_{\text{ph}}^5) \ . \tag{1.24}$$

The electron temperature is highly sensitive to input power. A thin metal film of volume 0.1 μm will increase from 0 K to 400 mK with a dissipated power of 1 pW [10]. Consequently, the significance of the weak emission power of electrons seen in (1.24) is that achieving electron temperatures below 100 mK requires large volumes of metal.

1.4 Piezoelectric Materials

1.4.1 Theoretical Background

What makes a material piezoelectric is essentially the arrangement of charges in the solid. Figure 1.3 compares piezoelectric and non-piezoelectric solids in 1-D.

For simplification, the central charges are fixed rigidly a distance $2l$ apart and all spring constants are identical.

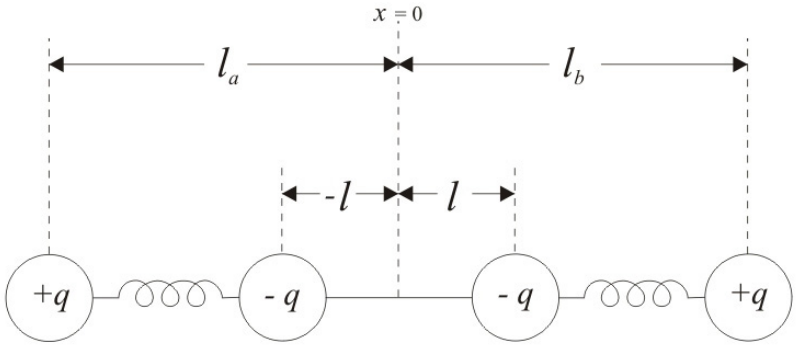

a) Model of a 1D *non-piezoelectric* solid

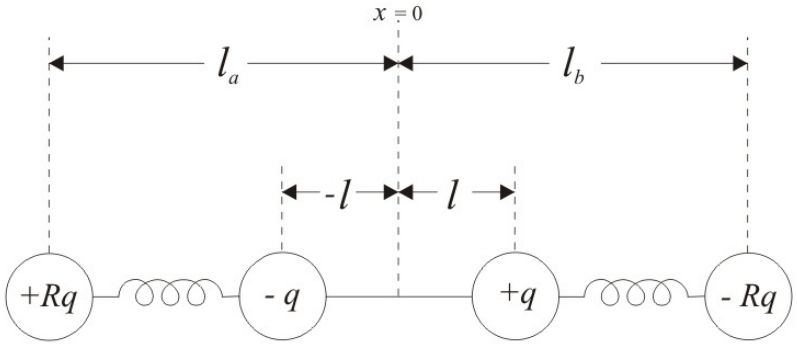

b) Model of a 1D *piezoelectric* solid

Figure 1.3: Comparison of piezoelectric and non-piezoelectric 1-D solids. Piezoelectric solids (b) are characterized by an antisymmetric charge distribution. (Figure adapted from Auld [13])

In a non-piezoelectric solid, the charge distribution is symmetric [13]. Figure 1.4 shows the effects of mechanical and electric forces on such a non-piezoelectric solid. The equations of interest are the mechanical response $\delta L = \delta l_b - \delta l_a$, or change in length, and the change in the total electric dipole moment $\delta P_x = q_n \delta x_n$. At equilibrium, as shown in Figure 1.3a, the polarization can be written

$$
\begin{aligned}
(P_x)_{equil} &= (q)(l_a) + \overbrace{(-q)(-l) + (-q)(l)}^{0} + (q)(l_b) \quad ; \quad l_a < 0 \\
&= q(l_a + l_b) \ , \qquad \text{where } -l_a = l_b = l_{eq} \\
(P_x)_{equil} &= 0 \ .
\end{aligned}
\tag{1.25}
$$

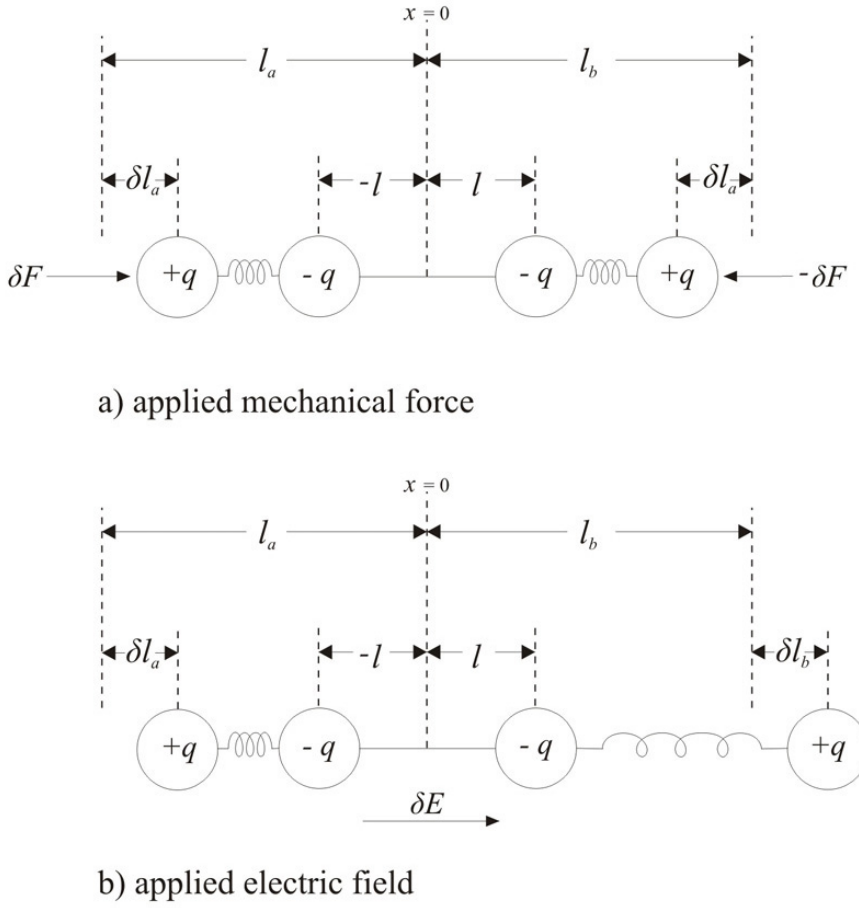

Figure 1.4: Effects of applying mechanical and electric forces on a non-piezoelectric solid. (Figure adapted from Auld [13])

In the 1-D example, a symmetric mechanical force applied to this solid results in a new charge distribution, but one that is again symmetric. Noting from Figure 1.4a that $-\delta l_a = \delta l_b$, the following is found for the change in polarization:

$$
\boxed{\delta P_x = q(\delta l_a) + q(\delta l_b) = 0 \ .}
\tag{1.26}
$$

As the symmetric charge distribution remains symmetric under mechanical forces, there is no change in the total electric dipole moment. Therefore, the non-piezoelectric solid does not exhibit an electric field response due to mechanical strain.

In the case of an electric field applied parallel to the 1-D lattice spacing, there will be an asymmetrical change in the charge distribution. For an electric force applied as in Figure 1.4b, the charges are displaced until they reach equilibrium such that

$$\begin{aligned} (F_a)_x + q\,\delta E_x &= 0 \\ (F_b)_x + q\,\delta E_x &= 0\ , \end{aligned} \tag{1.27}$$

Also in Figure 1.4b, we see that the applied electric field affects the identical charges such that $\delta l_a = \delta l_b$. Using the first relation in (1.25), we then find the change in polarization for the non-piezoelectric solid will be

$$\delta P_x = q\delta l_a + q\delta l_b = 2q\delta l_a\ . \tag{1.28}$$

The mechanical response, or change in length is then

$$\boxed{\delta L = \delta l_b - \delta l_a = 0\ .} \tag{1.29}$$

In a piezoelectric solid, the charge distribution is antisymmetric as seen in Figure 1.3b. The expression for polarization is thus written

$$\begin{aligned} (P_x)_{equil} &= (Rq)(l_a) + (-q)(-l) + (q)(l) + (-Rq)(l_b) \\ &= 2ql + Rq(l_a - l_b)\ , \qquad \text{where } -l_a = l_b = l_{eq} \\ (P_x)_{equil} &= 2q(l - Rl_{eq})\ . \end{aligned} \tag{1.30}$$

From Figure 1.5a we can see that, just as in the non-piezoelectric case, the application of a mechanical force results in changes of position for the charges such that $-\delta l_a = \delta l_b$. Thus, the change in polarization will be non-zero and is given by

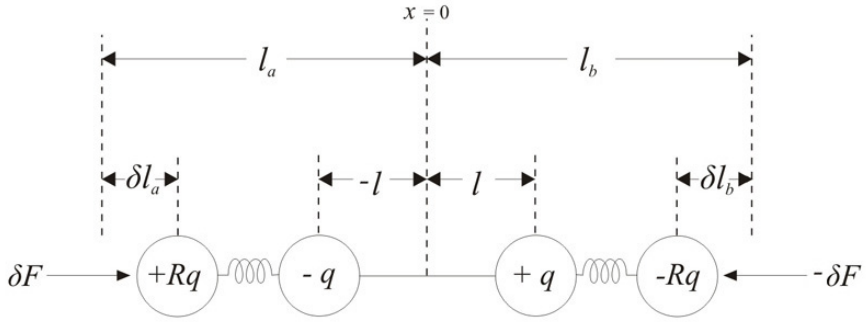

a) applied mechanical force

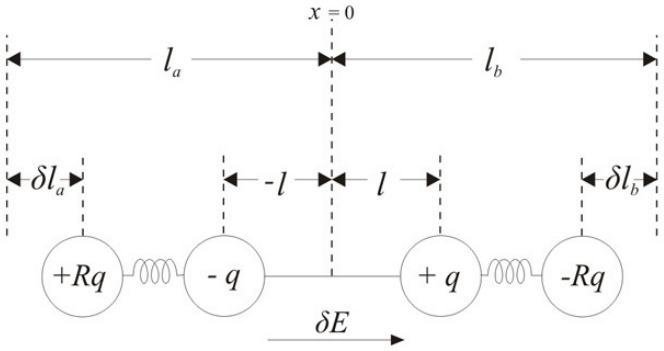

b) applied electric field

Figure 1.5: Effects of applying mechanical and electric forces on a piezoelectric solid. (Figure adapted from Auld [13])

$$\boxed{\delta P_x = Rq\delta l_a - Rq\delta l_b = 2Rq\delta l_a} \tag{1.31}$$

and the opposite signs on charges $+Rq$ and $-Rq$ will result in a symmetric response ($\delta l_a = -\delta l_b$) to the applied electric field as in Figure 1.5b, with a change in length given by

$$\boxed{\delta L = 2\delta l_a\ ,} \tag{1.32}$$

resulting in an electric response to a mechanical force and a mechanical response to an electric field as expected for a piezoelectric solid.

1.4.2 Acoustic Field Equations

To better understand the behavior of plane waves in piezoelectric solids, it is first necessary to outline the basic assumptions by reviewing the acoustic field equations [13]. The equation of motion is

$$\nabla \cdot \mathbf{T} = \frac{\partial \mathbf{p}}{\partial t} - \mathbf{F} \,, \tag{1.33}$$

where $\mathbf{p} = \rho \mathbf{v}$ is defined as the momentum density in kg/m^2 s, $\mathbf{F}$ is force, and $\mathbf{T}$ is the stress field. The strain-displacement relation can be written as

$$\nabla_s \mathbf{v} = \frac{\partial \mathbf{S}}{\partial t} \,, \tag{1.34}$$

where ∇_s is the symmetric displacement gradient operator. An analogy between these and the Maxwell equations can be drawn from the four basic field quantities $\mathbf{p}$, $\mathbf{v}$, $\mathbf{T}$, and $\mathbf{S}$, where the latter is the strain field. Taking $\mathbf{T}$, $\mathbf{v}$, $\mathbf{p}$, and $\mathbf{S}$ as equivalent to $\mathbf{E}$, $\mathbf{H}$, $\mathbf{B}$, and $\mathbf{D}$ respectively, it can be shown that the above equations (1.33) and (1.34) are analogous to the Maxwell equations:

$$-\nabla \times \mathbf{E} = \frac{\partial \mathbf{B}}{\partial t} \tag{1.35}$$

and

$$\nabla \times \mathbf{H} = \frac{\partial \mathbf{D}}{\partial t} + \mathbf{J}_c + \mathbf{J}_s \tag{1.36}$$

with $\mathbf{J}_c$ being the electric current density and $\mathbf{J}_s$ the source current density.

1.4.3 Quasistatic Approximation

By inspecting the propagation along a cube edge or face diagonal of a cubic piezoelectric medium with no losses, it can be shown that the piezoelectric coupling between electromagnetic and acoustic uniform plane waves is negligibly small

compared to the quasistatic electric field [13]. This important distinction provides a convenient method by which to calculate the electric potential in the form of the Christoffel equation.

Piezoelectric wave systems are characterized by two kinds of electric field distributions. Figure 1.6 shows a schematic of the polarizations for acoustic waves traveling along the x-axis.

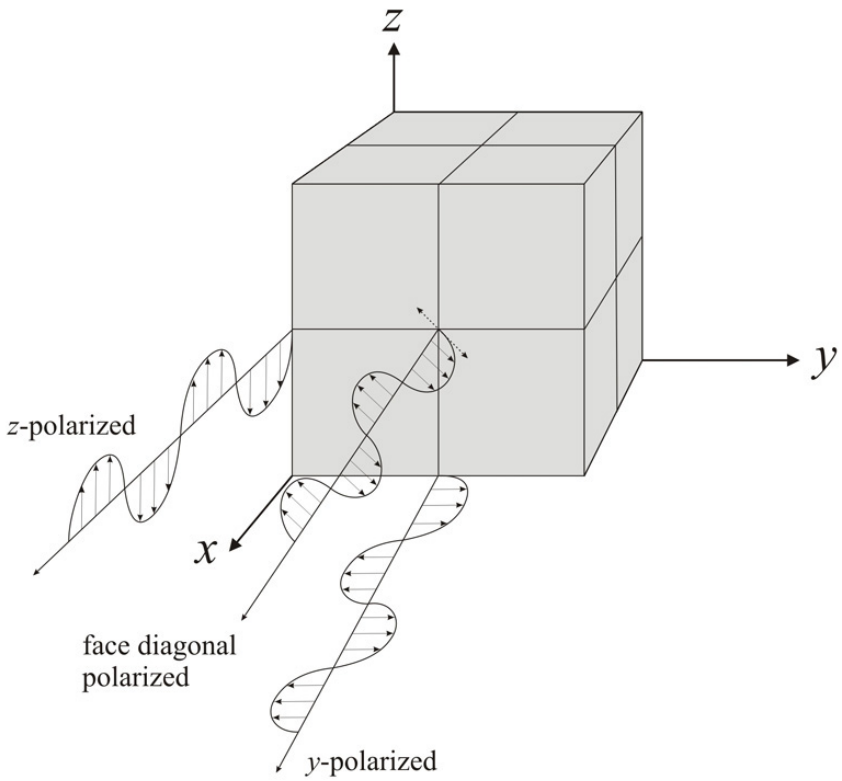

Figure 1.6: Polarizations of acoustic waves traveling along the x-axis.

Waves with cube edge (x, y, or z) polarized displacements are associated with fields in which $\nabla \times \mathbf{E} \neq 0$, called rotational fields $\mathbf{E}_r$, characteristic of electromagnetic waves. Waves polarized in the face diagonal direction (rotated 45° from the cube edge) have fields with zero curl [13] and can be described by the gradient of a scalar potential ($-\nabla\Phi$). As these fields are still time dependent, they are called quasistatic. The total field then becomes $\mathbf{E} = \mathbf{E}_r - \nabla\Phi$ and the coupled field equations for the piezoelectric medium of density ρ with no sources can be written

$$\nabla \cdot \mathbf{c}^E : \nabla_s \mathbf{v} \;=\; \rho \, \frac{\partial^2 \mathbf{v}}{\partial t^2} \;+\; \nabla \cdot \left[\mathbf{e} \cdot \frac{\partial (\mathbf{E_r} - \nabla \mathbf{\Phi})}{\partial t} \right] \tag{1.37}$$

and

$$-\nabla \times \nabla \times \mathbf{E} \;=\; \mu_0 \epsilon^S \cdot \frac{\partial^2 (\mathbf{E_r} - \nabla \mathbf{\Phi})}{\partial t^2} \;+\; \mu_0 \mathbf{e} : \nabla_s \frac{\partial \mathbf{v}}{\partial t} \;, \tag{1.38}$$

where $\mathbf{c}^E$ is the stiffness matrix at constant electric field E, $\mathbf{e}$ is the piezoelectric stress matrix, and ϵ^S is the permittivity matrix at constant strain S. The following convention is used here:

$$\mathbf{A} : \mathbf{B} = \sum_{ij} A_{ij} B_{ij} \;.$$

The stiffness matrix $\mathbf{c}^E$ describes the microscopic behavior of the solid as a collection of spring constants operating with respect to crystal axes. In this way, Hooke's Law can be written in matrix form to give a single expression taking into account all the Hooke's Law relations within the solid. Similarly, the piezoelectric stress matrix $\mathbf{e}$ describes the material response to electric and mechanical forces as a collection of piezoelectric constants and the permittivity matrix ϵ^S contains information about the material's dielectric properties. The generalized form of each matrix depends on crystal structure. A hexagonal crystal such as AlN for example, has a generalized piezoelectric stress matrix of the form [13]

$$[e_{ij}] = \begin{bmatrix} 0 & 0 & 0 & 0 & e_{x5} & 0 \\ 0 & 0 & 0 & e_{x5} & 0 & 0 \\ e_{z1} & e_{z1} & e_{z3} & 0 & 0 & 0 \end{bmatrix} \;, \tag{1.39}$$

where $e_{x5} = -0.48$ C/m^2, $e_{z1} = -0.58$ C/m^2, and $e_{z3} = 1.55$ C/m^2 in the case of wurtzite AlN [14]. The generalized forms of these matrices for common crystal structures can be found in the literature [13].

Now, neglecting the electromagnetic field coupling, equations (1.37) and (1.38) in abbreviated matrix form are

$$\nabla_{iK} c^E_{KL} \nabla_{Lj} v_i \; - \; \rho \, \frac{\partial^2 v_i}{\partial t^2} \; = \; -\nabla_{iK} e_{Kj} \nabla_j \frac{\partial \Phi}{\partial t} \tag{1.40}$$

and

$$-\nabla_i \epsilon^S_{ij} \nabla_j \frac{\partial^2 \Phi}{\partial t^2} \; = \; \nabla_i e_{iL} \left(\nabla_{Lj} \frac{\partial v_j}{\partial t} \right) \; , \tag{1.41}$$

where addition is over repeated subscripts and $[\nabla_i] \; = \; \left[\frac{\partial}{\partial x} \; \frac{\partial}{\partial y} \; \frac{\partial}{\partial z} \right]$.
For a uniform plane wave propagating along a direction $\hat{l} \; = \; \hat{x}_x + \hat{y}_y + \hat{z}_z$ in a material with no sources, the fields are of the form $e^{i(\omega t - k\hat{l}\mathbf{r})}$. The operators ∇_{iK} and ∇_{Lj} can then be written $-ik_{iK}$ and $-ik_{Lj}$ respectively. This allows a further reduction in the coupled wave equations such that

$$-k^2 (l_{iK} c^E_{KL} l_{Lj}) v_i \; + \; \rho \omega^2 v_i \; = \; i\omega k^2 (l_{iK} e_{Kj} l_j) \Phi \tag{1.42}$$

and

$$\omega^2 k^2 (l_i \, \epsilon^S_{ij} \, l_j) \Phi \; = \; -i\omega k^2 (l_i e_{iL} l_{Lj}) v_j \; . \tag{1.43}$$

Using (1.43), an expression can be written for the potential Φ in terms of particle velocity

$$\Phi = \frac{1}{i\omega} \frac{(l_i e_{iL} l_{Lj})}{l_i \, \epsilon^S_{ij} \, l_j} v_i \; . \tag{1.44}$$

Substituting this into (1.42), we get

$$k^2 \left(l_{iK} \left\{ c^E_{KL} \; + \; \frac{[e_{Kj} l_j][l_i e_{iL}]}{l_i \, \epsilon^S_{ij} \, l_j} \right\} l_{Lj} \right) v_j \; = \; \rho \omega^2 v_i \; , \tag{1.45}$$

which is the Christoffel equation with the term c_{KL} replaced by

$$\left\{ c_{KL}^{E} \; + \; \frac{[e_{Kj} l_j][l_i e_{iL}]}{l_i \, \epsilon_{ij}^{S} \, l_j} \right\} \; . \tag{1.46}$$

where the second term produces the piezoelectric interactions. This is known as the *piezoelectrically stiffened elastic constant*. Once a plane wave solution for $\mathbf{v}$ is found, the potential can be calculated using (1.44). For the hexagonal crystal, the permittivity matrix ϵ_{ij}^{S} and the elastic stiffness matrix c_{KL}, with constants for AlN, are given by

$$[\epsilon_{ij}^{S}] = \begin{bmatrix} \epsilon_{xx}^{S} & 0 & 0 \\ 0 & \epsilon_{xx}^{S} & 0 \\ 0 & 0 & \epsilon_{zz}^{S} \end{bmatrix} \quad ; \; \epsilon_{xx}^{S} = \epsilon_{zz}^{S} = 8.5\epsilon_0 \tag{1.47}$$

and

$$[c_{KL}] = \begin{bmatrix} c_{11} & c_{12} & c_{13} & 0 & 0 & 0 \\ c_{12} & c_{11} & c_{13} & 0 & 0 & 0 \\ c_{13} & c_{13} & c_{33} & 0 & 0 & 0 \\ 0 & 0 & 0 & c_{44} & 0 & 0 \\ 0 & 0 & 0 & 0 & c_{44} & 0 \\ 0 & 0 & 0 & 0 & 0 & \frac{1}{2}(c_{11} - c_{12}) \end{bmatrix} \; ; \; \begin{array}{l} c_{11} = 410 \text{ GPa} \\ c_{12} = 140 \text{ GPa} \\ c_{13} = 100 \text{ GPa} \\ c_{33} = 390 \text{ GPa} \\ c_{44} = 120 \text{ GPa} \end{array} \tag{1.48}$$

1.4.4 X-ray Characterization

Good piezoelectric properties of AlN require that the material be <002> oriented [15], meaning that the c-axis must be perpendicular to the substrate surface. The degree to which this orientation dominates is crucial in determining the piezoelectric response of the AlN film. An X-ray rocking curve (r-c) measurement is used to determine the angular distribution of the grains with respect to the surface. A sharp peak in the r-c measurement for a particular orientation of reflection indicates the dominance of that orientation compared to others. An

example r-c curve for the sample used in this study is shown in Figure 1.7 below.

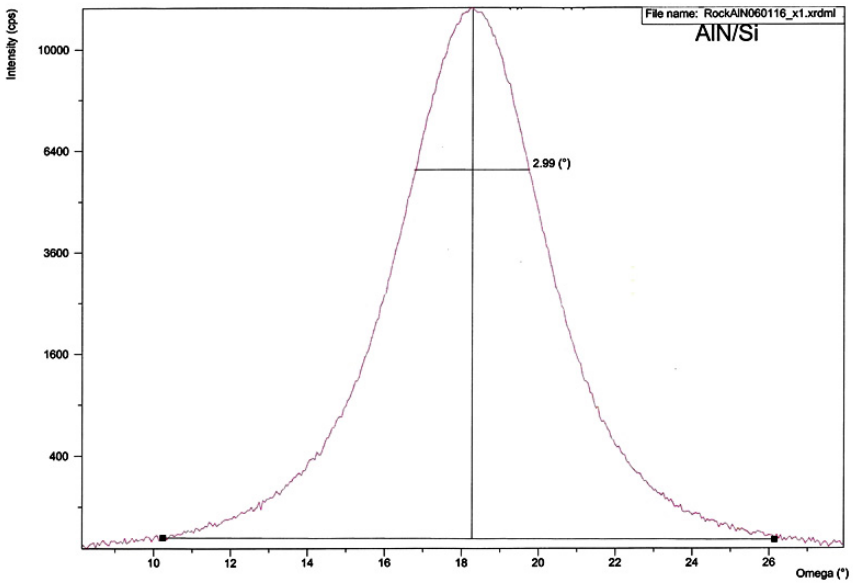

Figure 1.7: The X-ray diffraction rocking curve (r-c) can be used to characterize the piezoelectric response of materials such as AlN. A narrow r-c peak indicates the dominance of a particular crystal orientation, which is a primary characteristic of piezoelectric quality.

1.4.5 Applications of Piezoelectric Structures

Piezoelectric structures have been in commercial use for over 60 years [16]. Among the applications are oscillators, resonators, sensors, and actuators. The basic function of a piezoelectric actuator is the mechanical positioning of structures using the coupling between electric fields and strain. The actuation voltages and low current consumption of piezoelectric actuators make them attractive alternatives to methods such as thermal and electrostatic [17].

A resonator is typically a physical structure with mechanical resonances at certain frequencies [18]. Capacitive transduction resonators are limited in that they show large resistance to mechanical motion. Piezoelectric resonators comparatively have much smaller motional resistance and are thus extremely well suited for the

ultra-high frequency range. In the mobile and wireless industry, there is a great interest in band pass filters near 800 MHz and above [19]. Bulk acoustic wave (BAW) resonators, compared to surface acoustic wave (SAW) resonators, can be made very small using standard silicon techniques. They also exhibit better power handling characteristics than SAW filters. These filters are composed of a thin piezoelectric film which is electro-acoustically excited by an electrode. An acoustic reflector is often needed especially in the case of high frequency applications. The reflector minimizes energy losses by confining the acoustic excitations to the resonator.

BAW resonators are also often used in sensing applications such as the monitoring of thin film deposition. The quartz crystal microbalance (QCM) consists of a thin disk of quartz as a resonator sandwiched between two circular electrodes. A varying voltage across the electrodes causes deformation in the crystal and a resonance occurs as a result of reflections from the top and bottom surfaces. This resonant frequency is dependent on the mass of the resonator and thus, changes in the resonant frequency can be used to detect very accurately the adherence of particles on its surface. A 5 MHz QCM for example, has a mass sensitivity of $\sim$0.057 Hz cm^2/ng [18].

1.5 Equipment

1.5.1 E-Beam Lithography

Electron beam lithography is a standard tool for nanofabrication in which a focused beam of electrons is directed at a substrate coated with polymeric, electro-sensitive material. A common e-beam lithography machine consists of an electron microscope with either a home-made or factory installed accessory to automate the beam movement. The polymeric e-beam-resist can be either positive or negative. In a positive resist, the exposed regions become soluble due to breaking of the polymer bonds while in a negative resist, exposure to the electron beam induces polymer bonding. After exposure, the resist is treated chemically (devel-

oped) to remove the soluble portions while leaving the intended pattern intact. Due to the direct transfer of patterns in comparison with optical lithography using a mask, e-beam lithography can avoid the diffraction limit of light to allow much higher resolution patterns. While the beam width of the electrons is often on the order of nanometers, the actual width of pattern features is limited primarily by back-scattering of electrons within the resist material and from the substrate surface. Current e-beam machines generally have a limit of ~ 10 nm. Specifications for the Raith e-LiNE machine used here can be found in Appendix C.

1.5.2 Ultra-High Vacuum (UHV) Metal Evaporation

Thermal evaporation is done in an ultra-high vacuum (UHV) evaporator. Typical base pressures in UHV evaporation are $\leq 10^{-6}$ Torr [10]. The material to be deposited is heated until its vapor pressure is high enough that atoms begin to flow ballistically from it toward the target. This can be done for example by Joule heating whereby the material to be evaporated is placed in a crucible made of high temperature material, through which a DC current is passed. Another method uses a high voltage electron beam aimed at the source material in a water cooled crucible made of similarly high temperature material. In this method, incident electrons impart energy and heat the material until the required vapor pressure is reached. The ballistic flow of material from source to target allows line-of-sight masking, making it a convenient method for depositing metal wires on patterned photo-resists. Evaporated metal particles in such a system typically have a diameter of 2 - 5 Å and behave according to the kinetic theory of gases [20]. The Maxwell-Boltzmann distribution gives a mean free path $\langle\lambda\rangle$ which depends inversely on pressure and the square of particle diameter. Reducing the amount of collisions these particles experience, and thus increasing $\langle\lambda\rangle$, requires very high vacuum conditions.

1.5.3 ^{3}He – ^{4}He Dilution Refrigerator

The ^{3}He – ^{4}He dilution refrigerator works on the basis of phase separation between ^{3}He and ^{4}He [8]. At temperatures below 870 mK, there is a spontaneous separation of the isotopes into two phases in which a normal fluid phase rich in ^{3}He floats on top of a superfluid phase rich in ^{4}He. With decreasing temperature, the separation between the two phases increases. At absolute zero, it reaches a maximum with pure normal fluid ^{3}He floating on top of 6.4% ^{3}He in dilution. The entropy of superfluid ^{4}He is negligible and that of normal fluid ^{3}He is much lower than the dilute ^{3}He. A controlled cycle of mixing, diffusion, and condensing can be used to achieve cooling beyond the 4 K surrounding bath temperature of liquid helium. The dilute ^{3}He in ^{4}He can be thought of as a gas and in this way, the process of introducing more condensed normal fluid ^{3}He through the phase boundary into ^{4}He, is analogous to the evaporation of a liquid into a gas. In this process of dissolving into the superfluid, ^{3}He atoms absorb the heat of solution then diffuse through the ^{4}He. This mixture is pumped through sealed channels which are in contact with ^{4}He heat exchange gas to another chamber held at $\sim$ 0.6 K. At this temperature, the ^{3}He is evaporated out of the superfluid and pumped to a condenser, allowing it to be introduced once again into the ^{4}He mixing chamber.

In Figure 1.8, we see a typical schematic of a cryostat employing the ^{3}He dilution refrigerator [11]. Purified ^{3}He is pumped from a condenser at 1.5 K through the main flow impedance. This is the first step in pre-cooling of the ^{3}He. It continues down through the 0.7 K still for further pre-cooling. From here, it will pass through one or more heat exchangers and finally be injected into the mixing chamber. The ^{3}He will then pass through the phase boundary, absorbing heat, and diffuse through the ^{4}He. Osmotic pressure then pumps this mixture up through the heat exchanger, where it cools the incoming ^{3}He. At the still, the dilute mixture is exposed to a 0.7 K heater which evaporates the ^{3}He, leaving the ^{4}He behind.

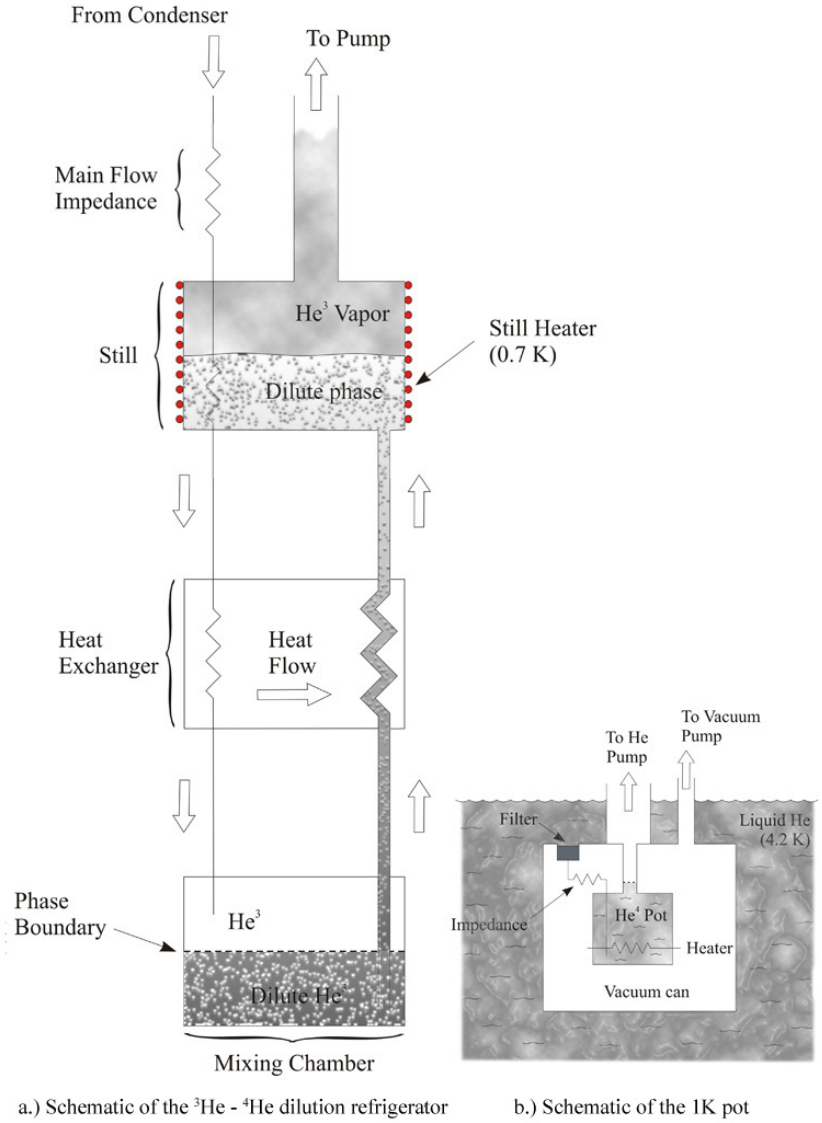

Figure 1.8: The basic functioning of a ^{3}He – ^{4}He dilution refrigerator is shown along with the design of the 1 K pot.

2 Fabrication

The combination of SINIS and SN junctions in the design requires evaporation and oxidation in multiple steps. While standard lithographic processes and equipment are used for the deposition of the metal wires, some slight modifications are required due to the specifics of our design. Sample rotation for metal evaporation and an iterative wet etch are the most significant modifications and will be described in the following sections. A schematic of the standard process is shown in Figure 2.1 below.

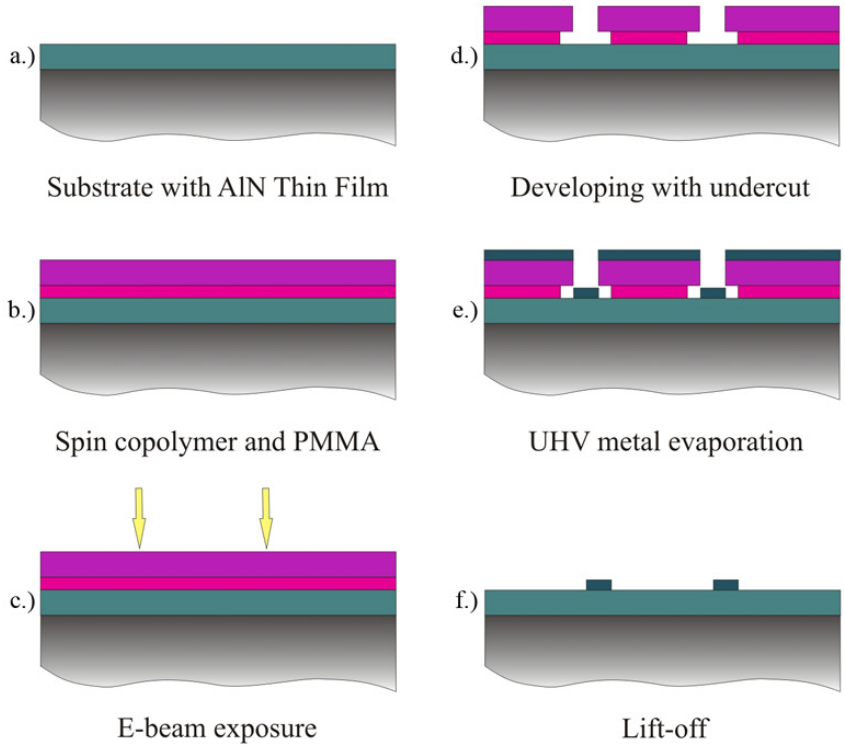

Figure 2.1: Process steps for lithography and deposition of metal wires for SINIS and SN junctions are shown. A thin coat of copolymer is used to create an undercut, preventing contact between the metal wire and the resist layers. This decreases the occurrence of residual edges and unwanted removal of metal wires during the lift-off process.

2.1 Sample Preparation

2.1.1 AlN Thickness Measurement

Prior to any processing, the thickness of the AlN film is measured using the Rudolph AutoEL III ellipsometer. These measurements are made at various points on the surface of the entire wafer to obtain a thickness gradient map. Figure 2.2 shows the thickness and refractive index data collected for the AlN sample used in this study. An average thickness of 556±3 nm is measured in the central region of the wafer. Some brief background on ellipsometer theory and a simplified user manual for the AutoEL can be found in Appendices A and B respectively.

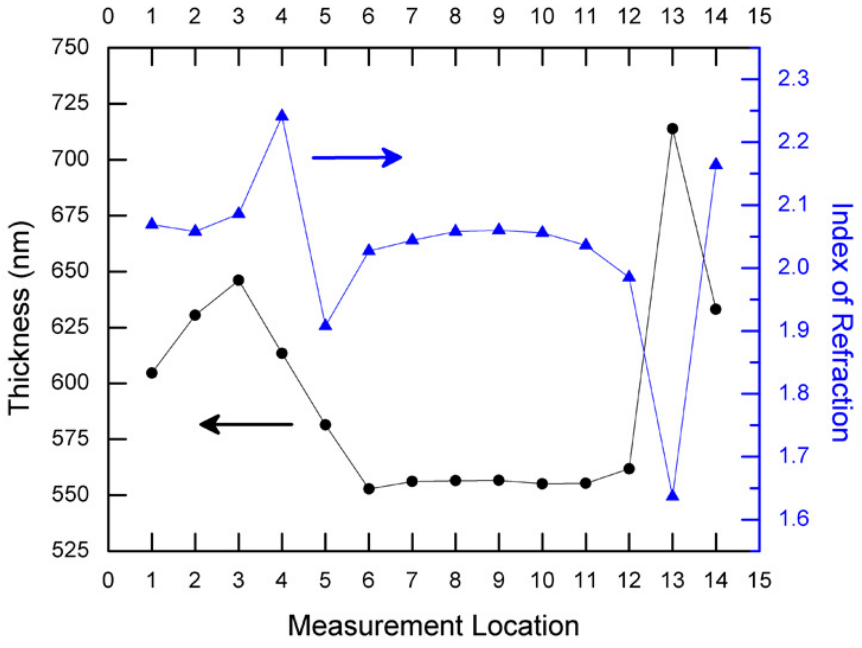

Figure 2.2: Thickness (black circles) and index of refraction (blue triangles) for the AlN sample used in this study are shown. Data points are taken along a diameter of the wafer approximately 5 mm apart.

2.1.2 Wafer Pre-cutting

The prefabricated Si wafer with sputtered piezoelectric AlN is first scored on the underside with an automated dicing saw. Grooves are cut 500 μm into the surface

with a spacing of 8 mm at right angles along the crystal orientation. This provides an accurate and convenient template from which to separate 8 mm × 8 mm chips to be used for sample fabrication. The chips can be separated easily with the fingers by rows and columns.

2.1.3 E-beam Resists

Resists used are polymethyl methacrylate 4% in anisole (PMMA A4) and copolymer methyl methacrylate and methacrylic acid P(MMA-MAA) 9% in ethyl lactate (EL 9). Copolymer EL 9 is spun at 6000 rpm for 55 seconds for a thickness of approximately 300 nm and baked at 90°C for 60 seconds. In baking multiple layers, it is important to consider the total time each layer spends on the baking plate. Lower layers should be baked minimally in order to avoid burning the resists such that it becomes difficult to lift off. The PMMA A4 resist is then spun at 1500 rpm for 55 seconds for a thickness of ∼300 nm and baked at 90°C for 60 s. The lower layer of copolymer is more sensitive to electron beam exposure than the PMMA on top and results in an undercut, or wider area of soluble material at the bottom as seen in Figure 2.1d. The use of such a copolymer sublayer adds physical separation between the deposited metal wire and the walls of PMMA, reducing the occurrence of residual metal edges and preventing unwanted removal of the wire during lift-off.

2.2 SINIS/SN Junctions

2.2.1 E-Beam Lithography

Patterning for the SINIS tunnel junctions is done using e-beam lithography with the Raith e-LiNE 50 system. Fine structures are patterned at 20 kV acceleration voltage using an aperture of 30 μm and a dosage of $\sim 140\mu$C cm^{-2}. The fine structure design is shown in Figure 2.3. Aperture and dosage for the larger structures leading to bonding pads are 120 μm and 100 μC cm^{-2} respectively. Acceleration voltage is kept at 20 kV. With the wider aperture, the larger structures

receive a higher current and thus, are patterned faster.

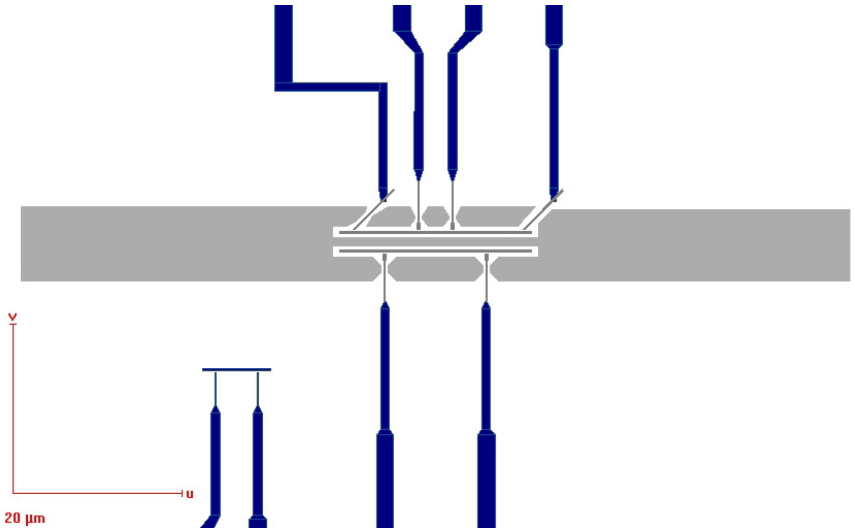

Figure 2.3: Fine structures for the SINIS and SN junctions. Line widths for the Al and Cu wires leading to the SINIS and SN junctions are 300 nm. Final gap used between emitter and receiver Cu wires is 3 μm. Grey areas indicate the etch pattern for release of the free-standing structures.

Line widths of the SINIS fine structure design are 200 nm and after developing, the final line width in the resist can be limited to less than 250 nm. This allows selective metalization by angled UHV evaporation as shown in Figure 2.4.

2.2.2 UHV Metalization

The angle and direction are chosen for a corresponding line-width such that metal will be deposited only along the length of pattern lines parallel to the direction of evaporation along the surface. Shadowing (Figure 2.5) prevents deposition across the width of perpendicular patterned lines.

Al wires for SINIS junctions are evaporated first at $\pm 60°$ from the normal of the sample surface. Opposing tilt angles are used to deposit the wires of the emitting and receiving SINIS junctions consecutively. 10 nm ± 0.1 nm of Al is evaporated at each angle with the overlap regions being approximately 1 μm from the junction edges. Chamber pressure is $2.5 \times 10^{-8} \pm 0.2 \times 10^{-8}$ Bar and deposition rate should be kept between 0.75 Å s^{-1} and 1.5 Å s^{-1} for best film quality and

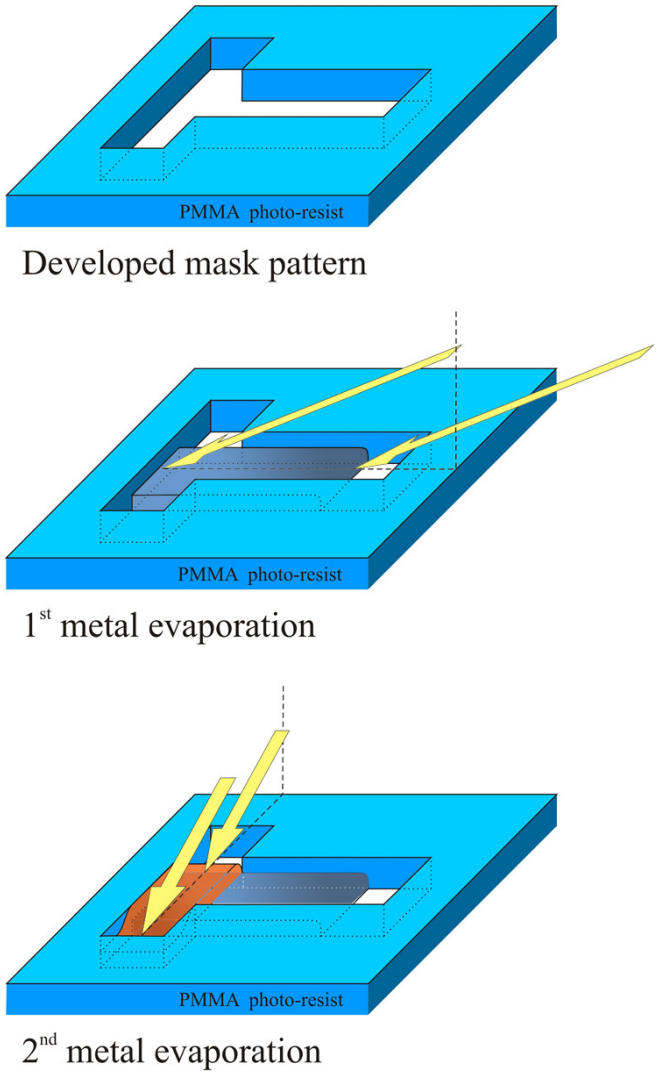

Figure 2.4: Selective metalization is achieved by angled and rotated UHV evaporation. The angle and direction of evaporation are chosen such that shadowing prevents deposition across the widths, or perpendicular sections, of patterned lines while allowing deposition along the lengths, or parallel sections of the pattern.

coverage. The sample is then brought into the UHV loading chamber, where the Al is oxidized at 40 mBar for 4 minutes. For the Cu evaporation, the sample must be rotated by 90°.

The previously deposited Al wires will produce shadows during Cu evaporation as shown in Figure 2.5. Therefore, this evaporation is divided into six stages with

alternating tilt angles of ±60°, depositing approximately 3.5 nm at a time. The alternating angles prevent breaks in the conduction path due to the shadowing.

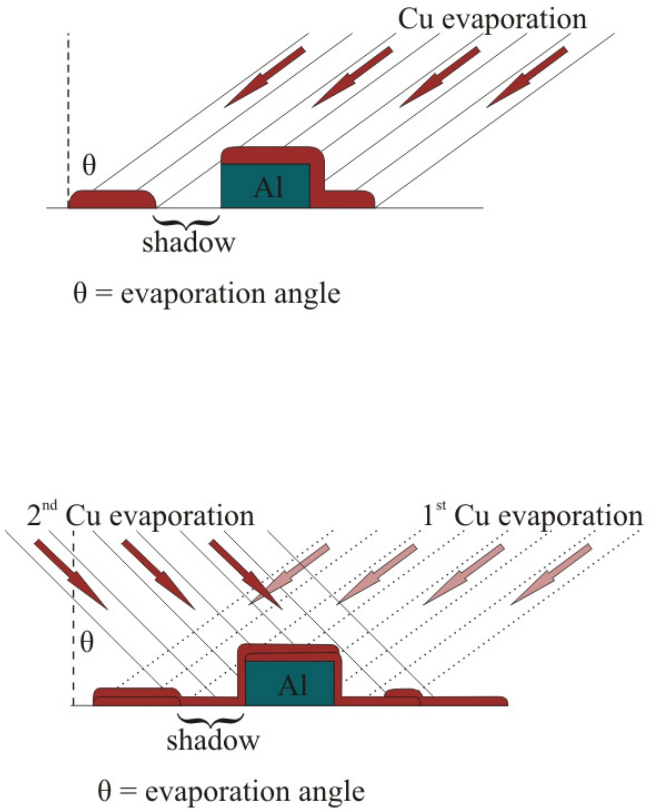

Figure 2.5: Previously deposited metal wires produce shadows in subsequent angled evaporations. Alternating angles are used to avoid breaks in the conduction path caused by shadowing.

Deposition rate for Cu is kept between 0.5 Ås^{-1} and 1.0 Ås^{-1} with the thickness of each evaporation being 3.4 nm ±0.1 nm resulting in a total thickness of 21 nm ±0.6 nm. The sample is then rotated once more by -45° to deposit the Al wires for the SN junctions. Deposition rate and pressure are the same as in the first Al evaporation, while tilt angle remains at 60°. Thickness of SN junction Al wires is increased to 40 nm, ensuring proper contact over the 20 nm Cu wire.

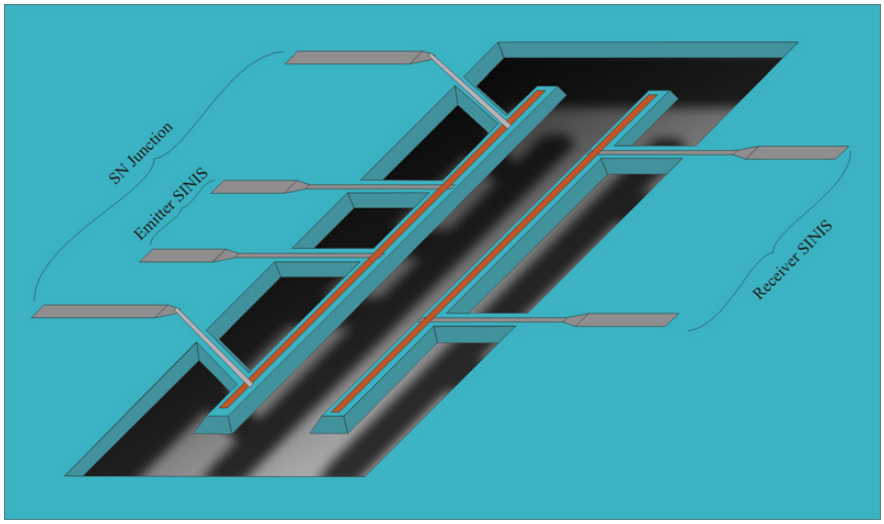

Figure 2.6: This schematic of the free-standing piezoelectric AlN supports with SINIS and SN junctions shows the idealized final measurement structure. On the emitting side are the SN junctions used to heat the copper wire. Temperature is measured on both the emitting and receiving side using SINIS junctions.

2.3 Free-Standing Piezoelectric Nanostructures

The pattern and release of the free-standing structures requires consideration of both design geometry as well as material components used in the SINIS and SN junctions. Figure 2.7 shows the general process for the release of free-standing structures. In the final structure, the SINIS and SN junctions are suspended on thin bridges over a cavity in the Si substrate of about 500 nm deep depending on the etch process and its length. The schematic seen in Figure 2.6 represents the idealized structure geometry. Initially realized structures are adjusted to allow greater tolerances for development of the fabrication process. The etch properties of Al and AlN tend to be similar and thus, it is necessary to develop an etch process which allows etching of AlN while leaving the Al wires of the junctions intact. A suitable resist is needed to ensure seamless coverage of the deposited metal wires. As our measurement scheme is highly sensitive to thermal conduction, it is also crucial to avoid or at least minimize any remaining materials used in etch masking, especially in the vicinity of the emitter and receiver junctions.

This turns out to be an important factor during cryogenic measurements as the differing thermal expansions of materials may lead to erroneous results as well as additional structural stresses.

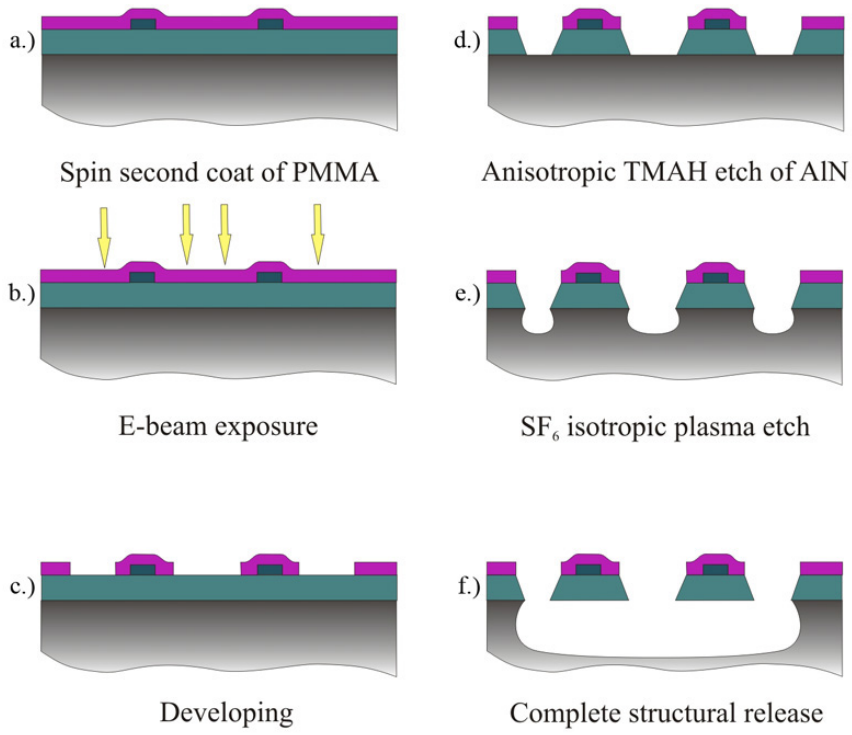

Figure 2.7: Process steps for lithography and release of free-standing piezoelectric structures requires accurate alignment with the existing pattern of metal wires. Proper adhesion of the resist is also crucial in providing adequate masking during the chemical etch of AlN.

It is known that tetra-methyl ammonium hydroxide (TMAH 25%) will etch AlN at a very high rate. TMAH is also selective to PMMA and thus presents a convenient masking option for etching the AlN patterns.

2.4 AlN Etching

2.4.1 Initial Etch

The relatively rapid etch rate of AlN in TMAH ($\gtrsim 8.3$ nm/s) somewhat complicates the process of finding the optimal etch time. It is found that 45 seconds is

generally sufficient to etch the bulk AlN for the desired pattern. After the TMAH bath, the sample is rinsed for another 30 seconds in deionized water. This initial bulk etching process leaves hillocks as seen in Figure 2.8.

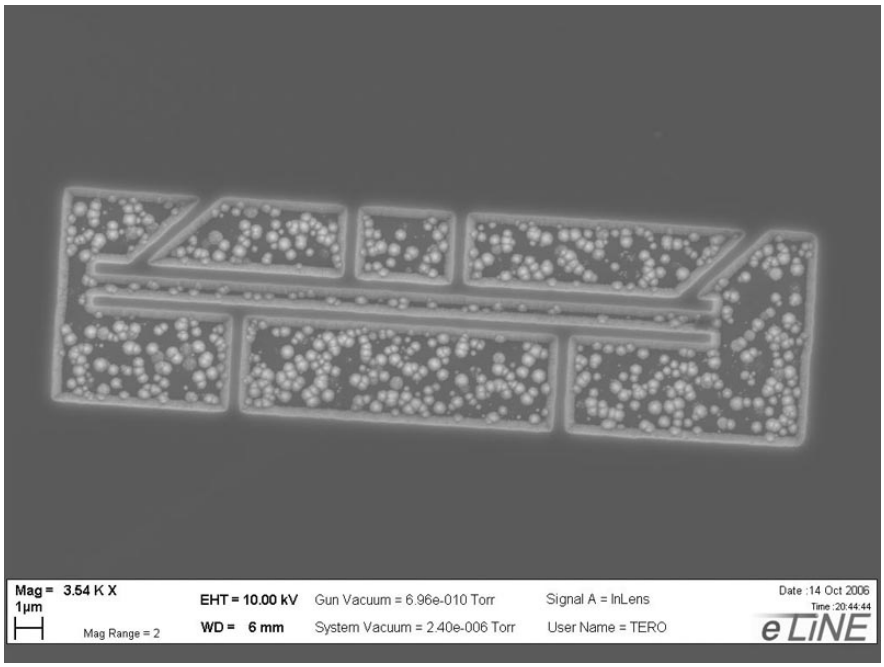

Figure 2.8: Insufficient TMAH etching of AlN is seen as residual hillocks between the masked regions. The lighter colored edges of the etched structures reveal a deviation from vertical etching. From the widening of structures, the etch angle is calculated to be approximately 30° from the vertical.

In the final structure, the SINIS and SN junctions are suspended on thin bridges over a cavity in the Si substrate of about 500 nm deep depending on the etch process and its length. A cryogenic reactive ion etch (RIE) at −100°C using SF_6 plasma will etch the Si substrate isotropically at a rate of ∼500 nm s^{-1} while a room temperature CHF_4 plasma etch will etch isotropically at ∼100 nm s^{-1}. The faster etch rate of the cryogenic SF_6 plasma is offset by the time taken to cool the RIE chamber. Achieving 1 μm clearance with SF_6 requires ∼45 minutes for cooling and 2–3 minutes for etching. The same clearance is achieved by room temperature CHF_4 plasma with approximately 20 minutes of etching. Due to heating of the sample stage by the plasma, the CHF_4 etch requires two etches with a short break to keep chamber conditions within parameter limits. Figure 2.9

shows the suspended structure without SINIS and SN junctions. It can be clearly seen that hillocks from the TMAH etch remain even after releasing the structures.

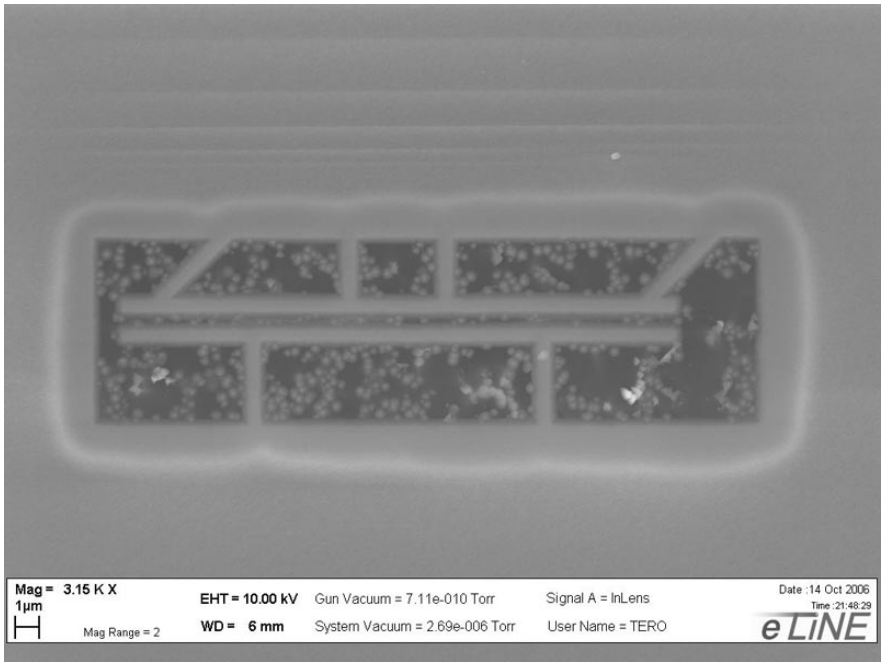

Figure 2.9: Residual hillocks are evident after the releasing of structures in a cryogenic SF_6 plasma etch. To achieve thermal isolation, these residuals require additional etch processing. Full release of the structures can be confirmed by the change in opacity along the outer edges of the cavity.

2.4.2 STEP Method

These hillocks pose obvious problems for proper thermal separation of the emitting and receiving SINIS junctions as well as in the reduction of thermal transport back to the bulk through the supporting structures. This issue can be resolved by introducing an iteration of secondary etch baths with a small amount of turbulence after the initial 45 second TMAH bath. The slightly turbulent etch process (STEP) involves re-immersion of the sample into the TMAH bath for approximately 10 - 15 seconds at a time while agitating the chip. This is immediately followed by a similarly turbulent rinse in deionized water. In order to ensure the remaining TMAH is cleared from the structures, this rinse can include the use of a syringe to increase the flow of deionized water at the surface. These STEP

iterations are effective in removing the residual hillocks from the etch pattern while being safe enough to leave the support structures unchanged. The success of this iterative process is likely due to the weak adhesion of the hillocks to the substrate surface. The short contact with turbulent TMAH is enough to release them without attacking the bulk AlN still protected by the PMMA mask. Depending on the length of the initial etch bath, some 4 - 6 STEP iterations of 15 seconds each are needed to sufficiently reduce hillocks. In this work, the primary concern is to remove all potential contacts between the emitting and receiving SINIS structures.

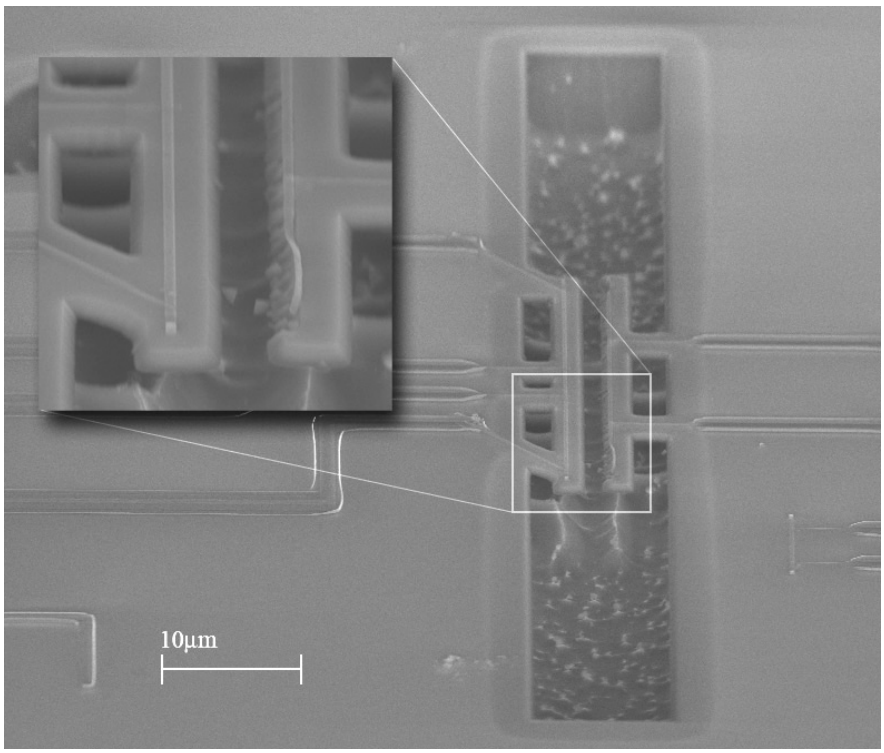

Figure 2.10: Full structural release of free-standing AlN bridges with SINIS and SN junctions intact. Success of the STEP method is seen in the lack of hillocks between emitter and receiver bridges and on the supporting structures leading to the bulk.

As is shown in Figure 2.10, the STEP method is successful in removing the residual hillocks left behind by the initial etch while leaving supporting structures with SINIS and SN junctions intact. These results indicate that while optimization

still poses several difficult challenges, the overall fabrication scheme is sound.

2.5 General Technical Challenges

There are several processing challenges specific to this project. Optimization of the fabrication of SINIS and SN junctions involves four primary considerations:

- Minimizing pattern time
- Optimizing line width
- Achieving proper lift-off
- Evaporation restrictions on geometry

Pattern time can be minimized by separating the fine structure from the larger electrical connects of the design. Nano-scale features of the metal wires and tunnel junctions are written using a writefield of 100 μm $\times$ 100 μm while the connections to the external leads are written with a 1000 μm $\times$ 1000 μm writefield. This simple adjustment of the image design reduces patterning time from approximately 15 min to just over 2 min. As we are patterning multiple designs on each chip, this leads to significant improvements in output. Considerations for line width are based on both proximity needs of the measurements as well as restrictions on thermal leakage. As seen in Figure 2.6, the heater and receiver are ideally very close and thus the line width needs to be reduced to prevent proximity exposure effects. Also seen in Figure 2.6 are the supporting legs for the emitter and receiver lengths. Reducing heat flow back to the bulk requires minimizing the width of these legs. The widening of patterned lines due to etch chemistry dictates a maximum width also for the superconducting wires. The piezoelectric AlN film is etched anisotropically at approximately 30° from the normal and results in a total widening of structures by about 600 nm with AlN thickness of 600 nm.

3 Preliminary Measurements

3.1 SINIS Calibration

The first measurements are performed to determine the characteristic electron-phonon (e-p) behavior on piezoelectric AlN films. This serves as the reference foundation on which thermal transport measurements are to be made. A schematic circuit diagram of the calibration measurement is shown in Figure 3.1.

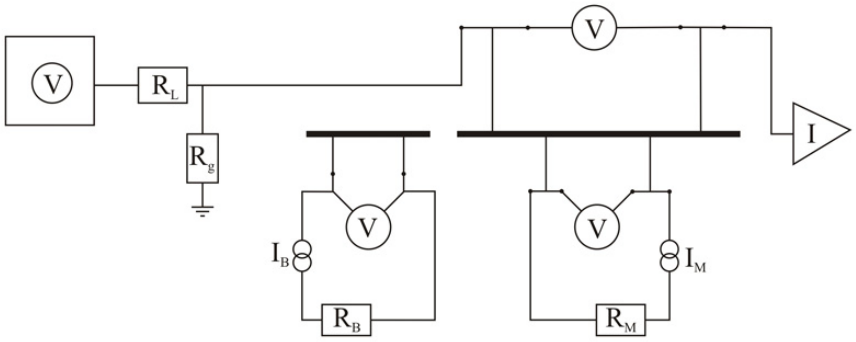

Figure 3.1: The circuit schematic for calibration measurements is shown. Thick horizontal lines represent the Cu wires.

Calibration curves are measured first by applying a bias current to the SINIS structures and decreasing the bath temperature slowly from approximately 1 K to the base temperature of 55 mK. One SINIS is used to measure the electron temperature between the SN junctions (electron SINIS). A separate SINIS is located horizontally in line with the first to measure the substrate temperature (substrate SINIS). The voltage response of each is recorded and fit to BCS theory curves. From this fit, the measured voltage can then be converted to temperature. Calibration data with corresponding BCS theory curves for the electron SINIS are shown in Figure 3.2. It can be seen that the data is in good agreement with BCS theory down to approximately 150 mK for a bias current of 125 pA and ∼250 mK for a bias of 375 pA. The plot also demonstrates the temperature sensitivity of the SINIS structure. With a low bias, it can be expected to give reliable temperature data as low as 150 mK.

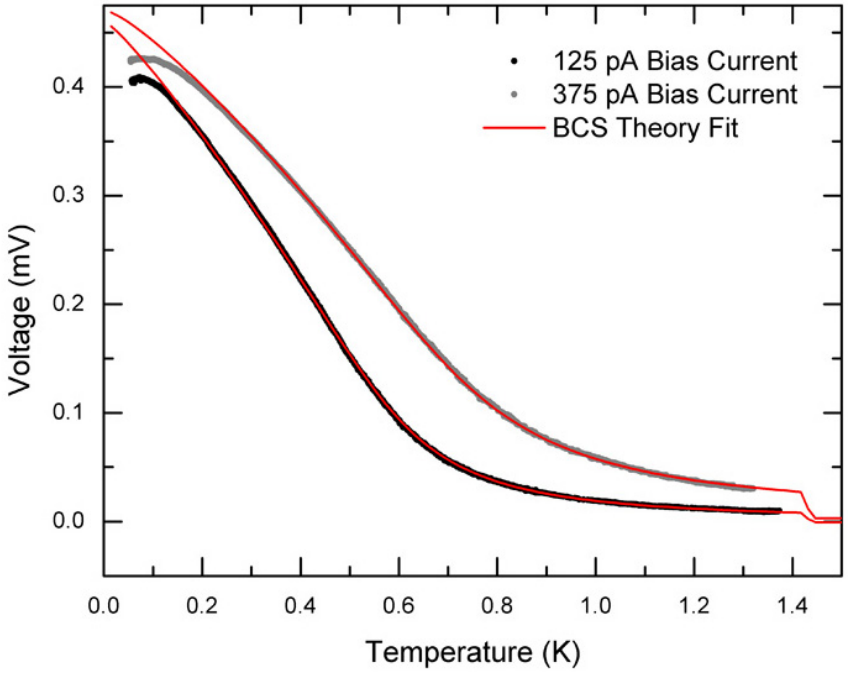

Figure 3.2: Calibration curves with corresponding BCS theory fits are shown for the electron SINIS at two bias currents, 125 pA and 375 pA.

3.2 I-V Characteristics

Next, the current-voltage (I-V) characteristics are observed for both the electron and substrate SINIS at a bath temperature of 56 mK. A circuit schematic for measuring the electron SINIS I-V characteristics is shown below.

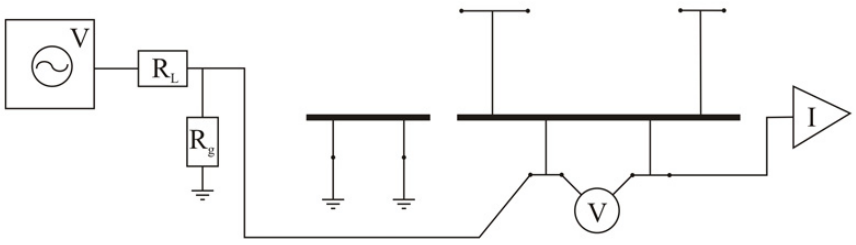

Figure 3.3: Circuit schematic for measuring I-V characteristics of the electron SINIS. Substrate SINIS leads are grounded to prevent interference while SN junctions on the heater side are left floating.

The I-V curves are measured by sweeping the voltage applied to the Cu wire via

those two junctions. Sweep time is 1770 seconds with extrema of ± 4 mV. The electron SINIS is employed in the middle of the Cu wire between the heating SN junctions while the substrate SINIS is positioned in line with the Cu wire approximately 1 μm away to measure the thermalized AlN film temperature. Positioning of this second SINIS ensures it is well thermalized with the bath. In this way, the temperature measured there can be used as an accurate reference. A SEM image of the reference sample in Figure 3.4 shows the locations of the SINIS and SN junctions.

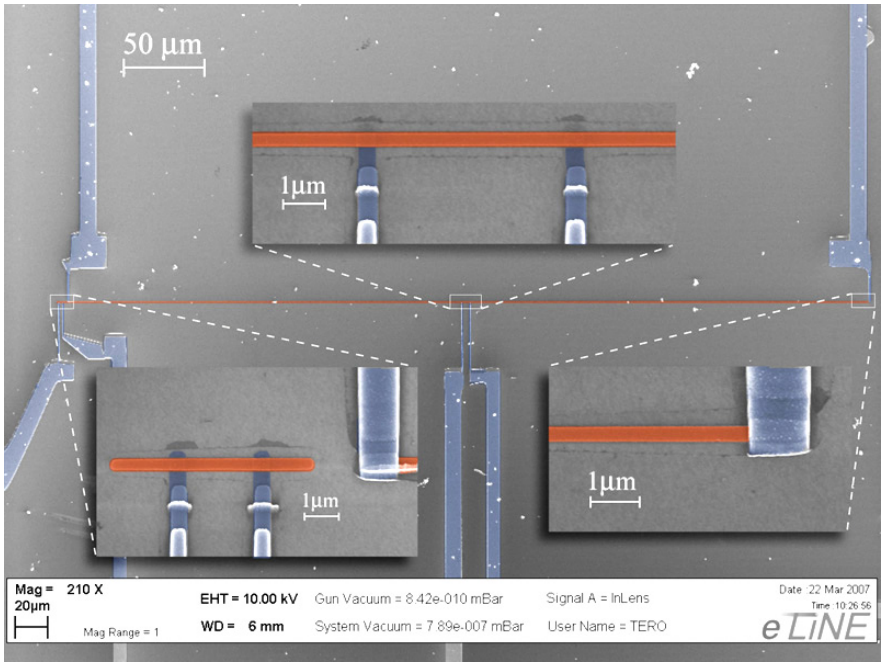

Figure 3.4: The reference sample is used to measure the electron-phonon coupling behavior on AlN thin films.

The electron SINIS I-V is shown in Figure 3.5. At higher voltages, the junction can be seen to approach simple resistive behavior indicated by the dashed red line. This gives the "normal-state" conductance G_N of the junction. From this data, we can also calculate the superconducting gap of the Al film. This is done by taking the derivative of the current with respect to voltage and plotting it against voltage. In Figure 3.6, we see the derivative plot with the band gap denoted by Δ and the normal-state or quasi-particle branch of the tunneling conductance

indicated by the dashed red line.

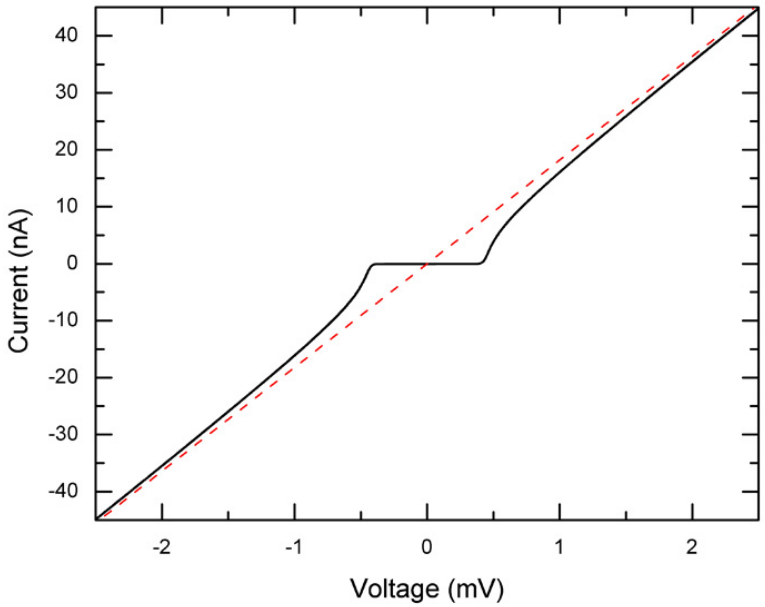

Figure 3.5: Electron SINIS current at 56 mK. At higher voltages, the junction approaches simple resistive behavior indicated by the dashed red line.

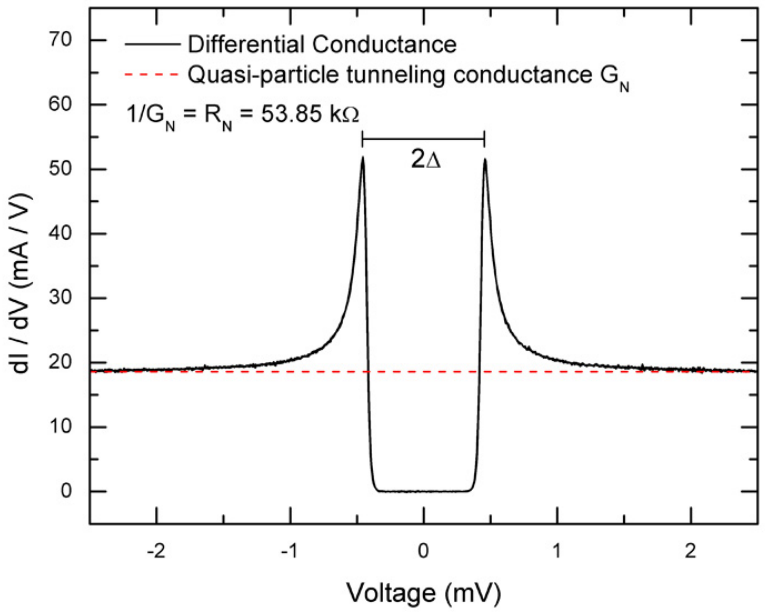

Figure 3.6: Plot of dI/dV for the electron SINIS. Dashed red line indicates the quasi-particle tunneling conductance.

A range of temperatures up to 1 K is investigated for the substrate SINIS. A circuit schematic for measuring its I-V characteristics is shown below.

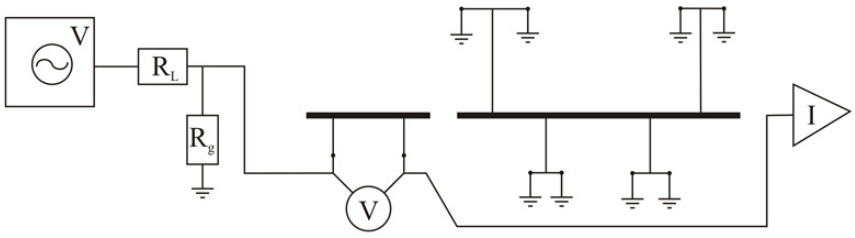

Figure 3.7: Circuit schematic for measuring I-V characteristics of the substrate SINIS. All leads to the heater side are grounded.

From these data, we can verify the temperature range and sensitivity at a given bias current.

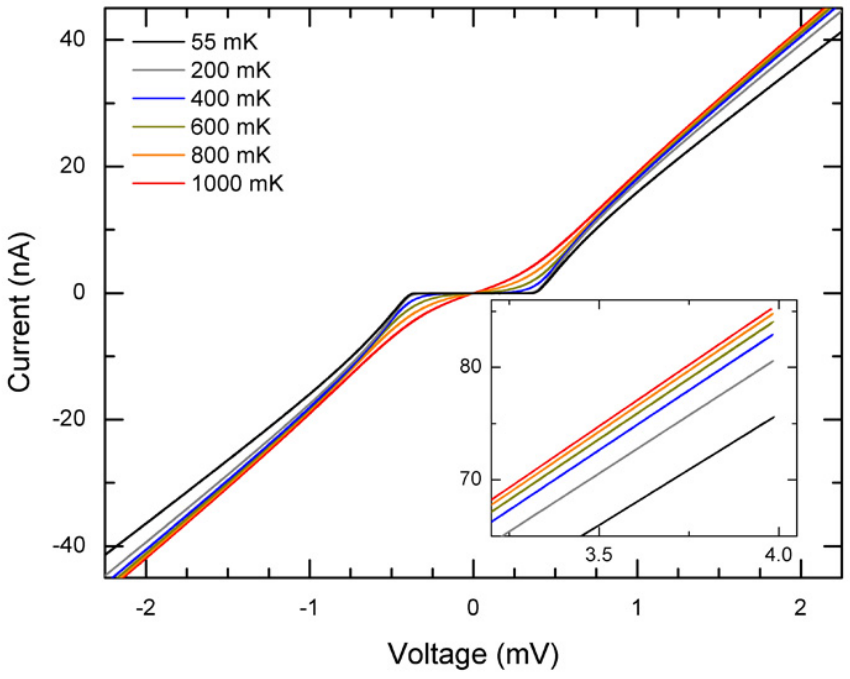

Figure 3.8: I-V characteristics for the substrate SINIS at varying temperature. Smoothing of the band gap edges at higher temperatures indicates the tendency toward normal metal behavior. Inset: Divergence of plots at higher voltages is thought to be the result of Coulomb blockade.

Figure 3.8 shows the I-V characteristics at each temperature investigated for the

substrate SINIS. It can be seen that increased temperature results in a rounding of the I-V curves at the edges of the band gap, indicating the tendency toward normal metal behavior as more electrons from the normal metal are excited to levels above the gap.

Divergence can be seen (inset Figure 3.8) in the quasi-particle tunneling currents at different temperatures in the substrate SINIS. This divergence is thought to be an indicator of Coulomb blockade [21]. The size of the normal metal island in the substrate SINIS is small enough that charging effects begin to affect the tunneling current. As expected, this is most prominent at lower temperatures. With the range narrowed in Figure 3.9, the same I-V curves demonstrate the temperature sensitivity of the 150 pA bias current.

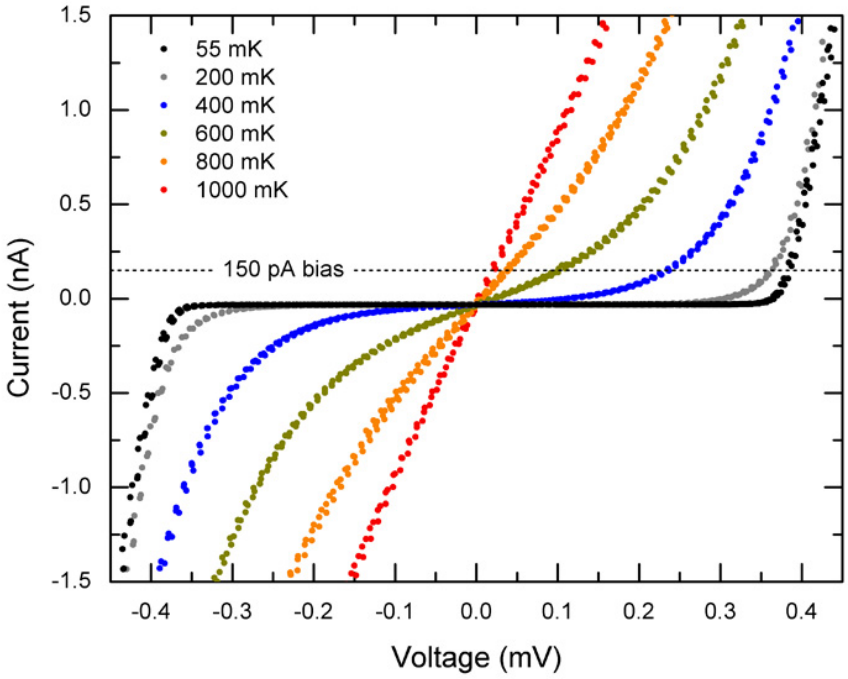

Figure 3.9: Narrowing the view on the I-V curves for the substrate SINIS shows the temperature dependence more clearly. At a given bias (e.g. 150 pA), the temperature sensitivity can be seen directly.

3.3 Electron-Phonon Cooling

By using the previously determined temperature calibration, we can calculate the temperature response in the Cu wire to the heating power applied through the SN junctions. The temperature dependence of energy transport by electrons is measured in the regime of hot electron scattering in a three dimensional phonon gas. Electrons in a Cu wire are heated using the slowly varying voltage applied over the SN junctions. Joule heating imparts a power P_{heat} to the electrons while the electrons transfer energy with a power P_{cool}. In ideal junctions, the current will flow unimpeded into the normal metal and out of the metal via Andreev reflection. The power loss through a non-ideal SN junction with normal state resistance R_N can be written as follows [22]:

$$P_{NS}(T_e) = \frac{2}{R_N e^2} \int_{-\infty}^{\infty} \epsilon[f_N(T_e) - f_s(T_s)][1 - A(\epsilon, Z) - B(\epsilon, Z)]\mathrm{d}\epsilon \ , \tag{3.1}$$

where $f_N(T_e)$ and $f_s(T_s)$ are the Fermi functions of the normal and superconducting metals respectively. The Andreev reflection coefficient $A(\epsilon, Z)$ and normal reflection coefficient $B(\epsilon, Z)$ are functions of energy ϵ and a dimensionless interface parameter Z related to the quality of the SN junction. These factors are given by

$$\begin{aligned} A(\epsilon, Z) &= \frac{\Delta}{E^2 + (\Delta^2 - E^2)(1 + 2Z^2)^2} \\ B(\epsilon, Z) &= 1 - A \ , \end{aligned} \tag{3.2}$$

when $E < \Delta$ and

$$\begin{aligned} A(\epsilon, Z) &= \frac{u_0^2 v_0^2}{\gamma^2} \\ B(\epsilon, Z) &= \frac{Z^2(Z^2 + 1)(u_0^2 - v_0^2)^2}{\gamma^2} \ , \end{aligned} \tag{3.3}$$

where $u_0^2 = 1 - v_0^2 = \frac{1}{2}[1 + (E^2 - \Delta^2)/E^2]$ and $\gamma^2 = [u_0^2 + Z^2(u_0^2 - v_0^2)]^2$ when $E > \Delta$ [23]. It can be seen from equation (3.2), that the term $[1 - A(\epsilon, Z) - B(\epsilon, Z)]$

appearing in the integral of the power loss equation (3.1) will be zero for $E < \Delta$. This means that no power will be lost in the heating of electrons in the normal metal even in the case of non-ideal SN junctions. The electron temperature of the normal metal can thus be measured with the SINIS junction to study the electron-phonon interaction. This method should also allow the observation of any effects that piezoelectric coupling might have on the e-p interaction.

Obtaining the e-p power emitted from the Cu wire requires taking into consideration the asymmetry imparted by the current biased SINIS junction between the two SN junctions. The current bias of this SINIS will oppose the input voltage during either the positive or negative portion of the voltage sweep and thus, cause an asymmetry. By adjusting the offset in SN current data between the positive and negative regions of the voltage sweep, this asymmetry is corrected.

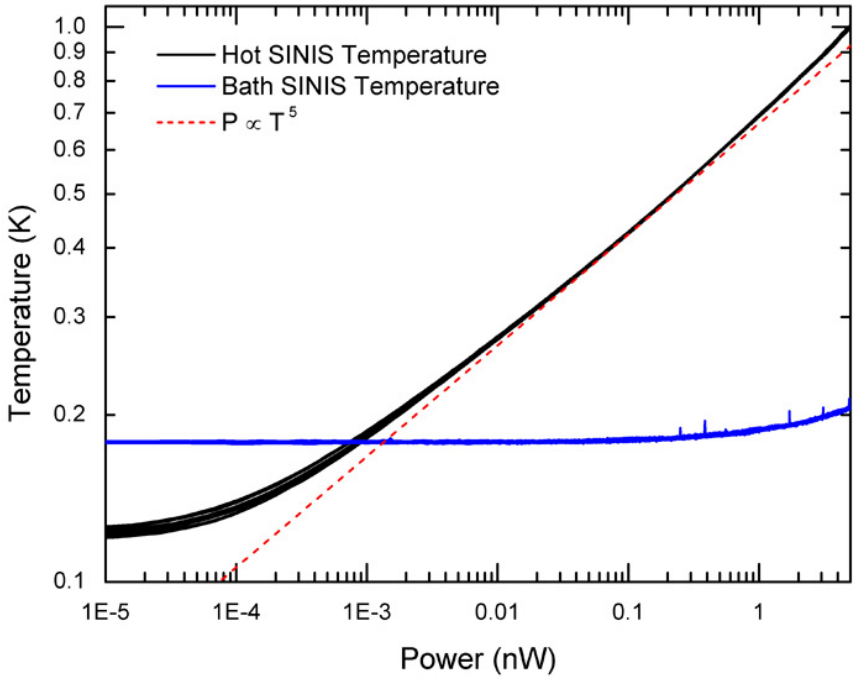

Figure 3.10: Temperature of both the electron and substrate SINIS is plotted against power input into the Cu wire. Between 0.01 nW and 1 nW, the electron heating power is closely approximated by a T^5 slope as shown by the dashed red line. Efficient thermalization with the substrate is confirmed for the substrate SINIS up to 0.1 nW heating power.

Temperatures for both the electron and substrate SINIS vs. power are shown in Figure 3.10. The substrate SINIS is extremely well thermalized with the substrate up to heating powers of 0.1 nW with significant heating seen only after ∼0.4 nW. The electron heating power for the electron SINIS is closely approximated by a T^5 power law between 0.01 nW and 0.1 nW as shown by the dashed red line. The electron-phonon coupling measurements thus reveal the expected $P \propto T^5$ dependence of temperature at the lower bias current with the behavior slightly modified at higher bias.

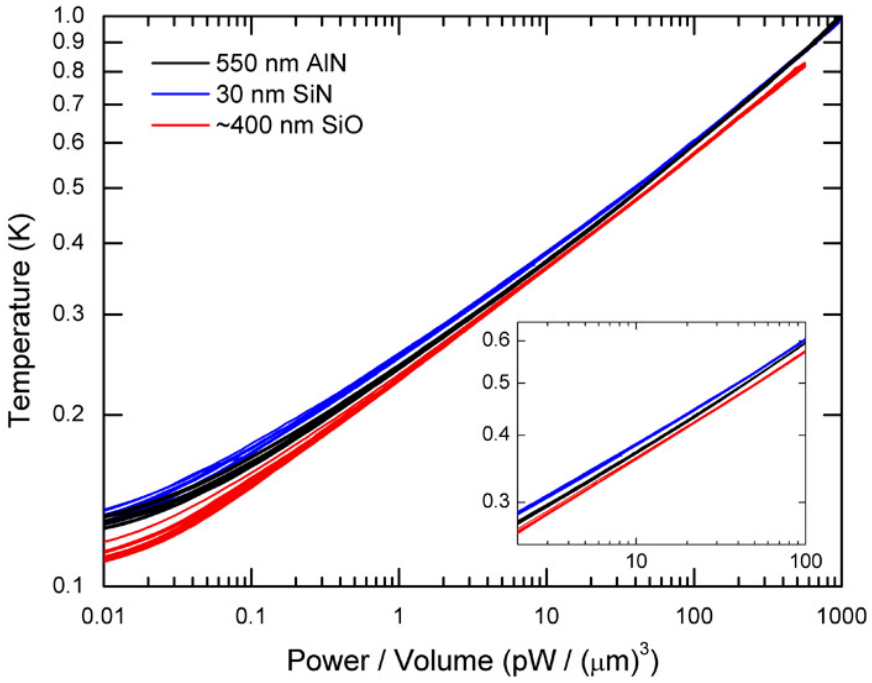

Figure 3.11: Temperature of the electron SINIS vs. power per unit volume is compared with similar SINIS junctions on SiN_x and SiO_2 films. All three junctions exhibit similar trends between 0.5 pW/μm^3 and 30 pW/μm^3. Cooling power of the AlN sample deviates from the trends of SiN_x and SiO_2 at higher temperatures.

In comparison with measurements of similar structures on SiO_2 and SiN_x thin films, the electron-phonon coupling behavior where $P \propto T^5$ is in reasonable agreement at intermediate power values (0.5 pW/μm^3 - 30 pW/μm^3). The similarity of trends can be seen in Figure 3.11. Temperatures are compared with power per

unit volume for previously measured samples on a SiO_2 film of approximately 400 nm and SiN_x with a thickness of 30 nm. At input power densities higher than 30 pW/μm^3, the AlN sample shows an increase in temperature response indicating that the relation $P \propto T^n$ changes such that $n < 5$. Determining whether this is the result of piezoelectric coupling requires further measurements on both piezoelectric AlN samples and non-piezoelectric nitrides of similar film thickness.

4 Conclusions

The goals of this project are the development and optimization of a fabrication scheme for the integration of tunnel junction devices with free-standing piezoelectric nanostructures for thermal transport studies. The design concept is demonstrated to be sound through each process step. Lithography of the tunnel junctions is optimized such that line widths can be restricted to a maximum of ∼300 nm with potential for optimization to below 100 nm. Metal evaporation and oxidation processes are demonstrated to output reproducible junction resistances in the range of a few tens of kΩ, reducing the effective noise in the measurement setup. Significant successes are achieved by iterative processes in the wet etching of AlN films such that well-defined structures are realized. The complete release of structures from the substrate is also demonstrated, resulting in free-standing piezoelectric nanostructures. Tunnel junctions are left intact and the initial emitter-receiver gap is well within the expected near-field limit.

Initial reference measurements indicate no significant deviation from previous measurements on non-piezoelectric films. Calibration curves are in good agreement with BCS theory fits and thus, the temperature sensitivity of SINIS junctions is as expected. While current-voltage (I-V) characteristics follow the usual behavior within the superconducting gap, there are some as of yet unexplained deviations in the results at higher voltages. A decrease is seen in the quasiparticle branch of tunneling current with increasing temperature. One candidate explanation being currently investigated is the possibility of Coulomb blockade effects occurring due to the small size of the normal metal island in these experiments. Electron-phonon cooling power is also shown to fall within the range of previous experiments. Temperature dependence is approximated closely by a $P \propto T^5$ relation. Further verification of reference measurements is in progress and the first measurements of the final design are to follow. Optimization of free-standing structure geometry as well as tunnel junction characteristics is required to achieve the final working design. A series of additional studies are planned

with the measurement gap between emitting and receiving bridge structures being varied in order to investigate the strength of the piezoelectric coupling. The sensitivity of this coupling to the measurement gap may provide the basis for displacement sensing devices. Modifications to the current structure geometry are also being developed for the fabrication of a piezoelectrically enhanced on-chip cooling device.

References

[1] J. Ullom, *Physics and applications of NIS junctions*, AIP conf. proc., **605**, 135–140, 2001

[2] M. Tinkham, *Introduction to Superconductivity*, International Series in Pure and Applied Physics, McGraw-Hill, New York, 1975

[3] J. Kivioja, *Mesoscopic Superconducting Tunnel Junction Devices*, Ph.D. thesis, Helsinki University of Technology, Espoo, Finland, Jun 2005

[4] H. Grabert and M. Devoret (Eds.), *Single Charge Tunneling: Coulomb Blockade Phenomena in Nanostructures*, *NATO Advanced Science Institute Series*, vol. 294, Plenum Press, New York, 1992

[5] F. Giazotto, T. Heikkilä, et al., *Opportunities for mesoscopics in thermometry and refrigeration: Physics and applications*, Reviews of Modern Physics, **78**, 217–274, Jan 2006, `cond-mat/0508093`

[6] J. Karvonen, L. Taskinen, and I. Maasilta, *Influence of Temperature Gradients on Tunnel Junction Thermometry below 1 K: Cooling and Electron-Phonon Coupling*, Journal of Low Temperature Physics, **146**(1/2), 213–226, Jan 2007

[7] L. Taskinen, J. Kivioja, J. Karvonen, and I. Maasilta, *Direct measurement of the electron-phonon relaxation rate in thin copper films*, Phys. Stat. Solid C, **1**(11), 2856–2859, 2004

[8] C. Bailey (Ed.), *Advanced Cryogenics*, The International Cryogenics Monograph Series, Plenum Press, London, 1971

[9] C. Kittel, *Introduction to Solid State Physics*, 7 ed., John Wiley and Sons, New York, 1996

[10] A. Cleland, *Foundations of Nanomechanics*, Springer, Berlin, 2003

[11] F. Pobell, *Matter and methods at low temperatures*, 2 ed., Springer, Berlin, 1996

[12] A. Sergeev and V. Mitin, *Electron-phonon interaction in disordered conductors: Static and vibrating scattering potentials*, Phys. Rev. B, **61**(9), 6041–6047, Mar 2000

[13] B. Auld, *Acoustic Fields and Waves in Solids*, vol. 1, 2 ed., Krieger Publishing Company, Malabar, Florida, 1990

[14] G. Bu, D. Ciplys, et al., *Electromechanical coupling coefficient for surface acoustic waves in single-crystal bulk aluminum nitride*, Applied Physics Letters, **84**(23), 4611–4613, Jun 2004

[15] E. Iborra, A. Sanz-Hervas, et al., *Assessment of the piezoelectric response of sputtered AlN films by x-ray diffraction*, IEEE Ultrasonics Symposium, **3**, 1808–1811, Sep 2005

[16] G. Iriarte, *AlN Thin Film Electroacoustic Devices*, Ph.D. thesis, Uppsala University, Uppsala, Sweden, 2003

[17] J. Olivares, E. Iborra, et al., *Piezoelectric actuation of microbridges using AlN*, Sensors and Actuators A, **123-124**, 590–595, 2005

[18] S. Humad, *Piezo-On-Silicon Microelectromechanical Resonators*, Master's thesis, Georgia Institute of Technology, Atlanta, Georgia, Jul 2004

[19] H. Loebl, C. Metzmacher, et al., *RF Bulk Acoustic Wave Resonators and Filters*, Journal of Electroceramics, **12**, 109–118, 2004

[20] A. Lindell, *Nanofabrication by Atomic Force Microscopy, Electron Beam Lithography and Reactive Ion Etching*, Ph.D. thesis, University of Jyväskylä, Jyväskylä, Finland, Aug 2000

[21] G. Falci, V. Bubanja, and G. Schön, *Quasiparticle and Cooper pair tunneling in small capacitance Josephson junctions*, Z. Phys. B, **85**, 451–458, 1991

[22] T. Hoss, C. Strunk, et al., *Multiple Andreev reflection and giant excess noise in diffusive superconductor/normal-metal/superconductor junctions*, Phys. Rev. B, **62**(6), 4079–4085, Aug 2000

[23] G. Blonder, M. Tinkham, and T. Klapwijk, *Transition from metallic to tunneling regimes in superconducting microconstrictions: Excess current, charge imbalance, and supercurrent conversion*, Phys. Rev. B, **25**(7), 4515–4532, Apr 1982

[24] Rudolph Research, *AutoEL-III Automatic Ellipsometer Instruction Manual*, Rudolph Research, Fairfield, N.J., 1982

A Ellipsometer Theory - AutoEL III

Incident and reflected beams are set at a fixed angle with respect to the sample. A compensator is placed between the source and sample, resolving the linearly polarized light into elliptically polarized light composed of two orthogonal components called the fast and slow axes. The compensator is constructed such that the slow axis component is shifted one quarter wave (90°) behind the fast axis. This phase shift will result in a polarization state differing from the input beam. An input polarization axis of 45° relative to the compensator will result in circularly polarized output light while any other angle will result in elliptically polarized output.

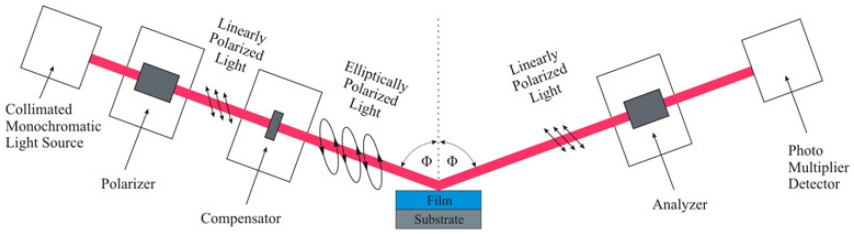

Figure A.1: Schematic of an automatic ellipsometer. A collimated beam of monochromatic, unpolarized light from the source passes through a polarizer and compensator slide, resulting in elliptically polarized light incident on a sample. After reflecting from the thin film surface, the polarization and intensity of the beam are measured by an analyzer and photo-multiplier respectively.

The azimuth (orientation of the major axis with respect to the plane of incidence) and ellipticity (ratio of minor to major axis) are controlled by the rotating polarizer. Light reflected from the sample surface will arrive at the analyzer with a different polarization state from the incident beam. When the reflected beam is anything other than circularly polarized, rotation of the analyzer will detect a change in photocurrent. This current will have two minima at analyzer azimuths 180° apart. When the reflected beam is linearly polarized, these minima correspond to full extinction. This condition is obtained by alternately changing the

polarizer and analyzer azimuths until true extinction is found. The ellipsometer determines the polarizer azimuth P at which the reflected beam is linearly polarized and the analyzer azimuth A at which its transmission axis is 90° to the linearly polarized reflected beam.

The ellipsometer measures changes in the polarization state of collimated, monochromatic polarized light[24]. This change in polarization is caused by reflection of the beam from a thin film surface. Collimated beams of monochromatic light can be represented by the following equation:

$$E(t) = Ee^{i\omega t}e^{i\epsilon} \ , \tag{A.1}$$

where ω is the frequency of light, E is the complex instantaneous amplitude, and ϵ is the time-independent phase. From classical optics, the angle of reflection Φ_r with respect to a normal to the surface at the point of incidence will be equal to the angle of incidence $\Phi_i = \Phi$.

The electric field of both incident and reflected beams can be represented by two orthogonal components of linear polarization **p** and **s** representing the components parallel and perpendicular to the plane of incidence respectively. Reflection from a surface will generally cause changes in relative phase and amplitude of **p** and **s** components. From these changes, two angles Δ and Ψ will be defined.

For the incident wave, E_p, E_s, $|E_p|$, $|E_s|$, ϵ_p, and ϵ_s are the complex amplitude, real time-independent amplitude, and time-independent phase of **p** and **s** components respectively. The reflected wave is indicated by primes (E'_p, $|E'_s|$, etc.). Reflection coefficients are then defined by

$$r_p \equiv \frac{E'_p(t)}{E_p(t)} \quad \text{and} \quad r_s \equiv \frac{E'_s(t)}{E_s(t)} \ . \tag{A.2}$$

From (A.1) we get

$$r_p = \frac{|E'_p|}{|E_p|}e^{i(\epsilon'_p - \epsilon_p)} \quad \text{and} \quad r_s = \frac{|E'_s|}{|E_s|}e^{i(\epsilon'_s - \epsilon_s)} \ . \tag{A.3}$$

The ratio of r_p and r_s is what the ellipsometer measures. This is given by

$$\rho = \frac{|E'_p||E_s|}{|E'_s||E_p|}e^{\left[(\epsilon'_p - \epsilon'_s) - (\epsilon_p - \epsilon_s)\right]} \ . \tag{A.4}$$

To simplify this, we define the following:

$$\tan\Psi_i = \frac{|E_p|}{|E_s|} \quad \text{and} \quad \tan\Psi_r = \frac{|E'_p|}{|E'_s|}$$
$$\Delta_i = \epsilon_p - \epsilon_s \quad \text{and} \quad \Delta_r = \epsilon'_p - \epsilon'_s \ ,$$

then (A.4) can be written

$$\rho = \frac{\tan\Psi_r}{\tan\Psi_i} e^{i(\Delta_r - \Delta_i)} \ , \tag{A.5}$$

and finally, if we let

$$\tan\Psi \equiv \frac{\tan\Psi_r}{\tan\Psi_i} \quad \text{and} \quad \Delta \equiv \Delta_r - \Delta_i \ ,$$

then (A.5) simplifies to

$$\rho = \tan\Psi e^{i\Delta} \ . \tag{A.6}$$

This is called the basic equation of ellipsometry.

The equations relating polarizer and analyzer azimuths to the values Δ and Ψ are as follows:

$$\Delta = 2P - 90^\circ \quad , \quad 2P - 270^\circ \quad , \quad (2m-1)90^\circ \pm 2P \quad ; \quad (m = 1, 2, 3, 4)$$

$$\Psi = A \ , \ 180^\circ - A \ .$$

A simplification is achieved by fixing the compensator to 45° and restricting the ranges of P and A to the following ranges named by convention zones 2 and 4:

$$\text{zone 2:} \quad -45^\circ \leq P_2 \leq 135^\circ \qquad 0^\circ \leq A_2 \leq 90^\circ$$
$$\text{zone 4:} \quad -135^\circ \leq P_4 \leq 45^\circ \quad -90^\circ \leq A_4 \leq 0^\circ \ .$$

The equations relating Δ and Ψ to P and A are then

$$\Delta_2 = 270^\circ - P_2 \quad , \quad \Psi_2 = A_2$$

and

$$\Delta_4 = 90^\circ - 2P_4 \quad , \quad \Psi_4 = -A_4 \ .$$

B Simplified AutoEL III Manual

Powering On and Stage Controls

Minimum operating accuracy requires laser to be on for ∼30 min. before use.

It is recommended that the ellipsometer be left on if more measurements are to be done.

Turn on the power using the switch located to the left of the ellipsometer (AutoEL).

Flip open the control panel

During warm-up is a good time for first time users to get a feel for the stage controls.

Insert a sample to align the spot in the eyepiece.

Side tilt: The two wheels on either side of the stage tilt as shown in the diagram.

Forward tilt: The wheel at the front tilts in the vertical plane perpendicular to side tilt.

Height: The large wheel at the bottom controls the height of the stage. (This should require very little adjustment)

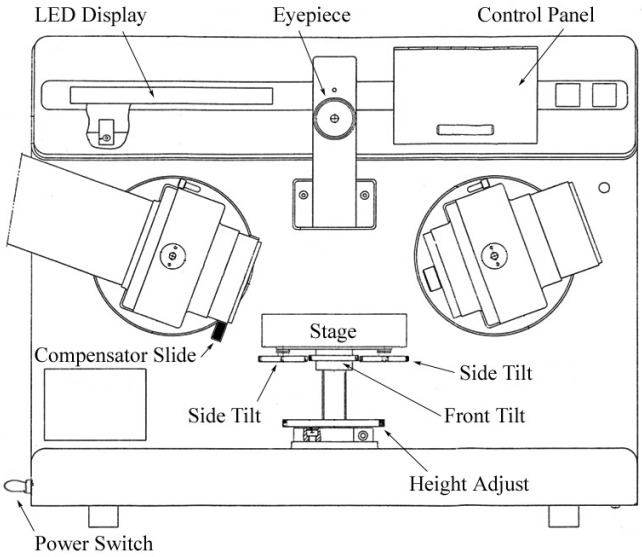

Figure B.1: Diagram of the AutoEL III ellipsometer.

AutoEL Initialization

Once the AutoEL is warmed up, note that the display should read:

```
UP COMP - INSERT SAMPLE - PRESS CONT
```

Push the *compensator slide* to the up position

Place the initial sample on the stage and **align it** using the Side Tilt wheels so that the light in the eyepiece is centered .

Check that the reflected beam enters the sensor aperture as close to center as possible, making small height adjustments if necessary (Large wheel at base of stage).

press `CONT`

The display will read:

```
AUTO EL III INITIALIZING REV. ###
```

Where `###` is the software version

To minimize errors caused by sample, use a well known single layer sample on Si substrate.

Other errors most frequently occur if the reflected beam does not correctly enter the analyzer.

Once initialization is complete, the display will read:

```
DOWN COMP - PRESS CONT OR PROG
```

Push the *compensator slide* to the down position.

Entering the Program

Measuring programs are chosen by entering a six digit code.

Press `PROG`.

Enter the six digit program code for your measurement.

Some frequently used codes can be found on the next page.

After entering the six digit code, **press** `E` (for enter) on the keypad.

To repeat the same measurement program, simply **press** `CONT`

Results are displayed as follows: TL NL ORD, where ORD is the thickness multiple.

$$\text{Final Thickness (Å)} = \text{TL} + (n \text{ x } \texttt{ORD}); \quad n = 0,1,2,\ldots$$

Make sure to check alignment if the sample has been moved and when a new sample is to be measured.

Numerical Entry

To clear the screen at any time, **press** `C` on the keypad.

To enter a decimal in a number, **use the** `D` **key**. (Ex. 4.2 press `4 D 2`)

Table 1: Some common single and double film measurement programs: TU, TL = layer thickness (upper, lower), NU, NL = index of refraction (upper, lower). Subscript i indicates initial estimate value. (all thickness values in Å)

Prog. Code	Measured Value	User Entered Value
210000	TL, NL	
211000	TL	NL
221000	TU	NU , NL , TL
222000	TU, NU	NU_i, NL , TL
223000	NL, TU	NU , NL_i, TL
227000	TL, TU	NU , NL , TL_i

C Raith e-LiNE

General Information

- Electron beam lithography: min. feature size < 20 nm
- High resolution SEM imaging: resolution < 10 nm
- Maximum sample size:

Key Specifications

Property	Measured	Factory Spec
Filament	Schottky TFE	
Beam size	1.8 nm @ 20 keV	2 nm @ 20 keV
	3.5 nm @ 1 kev	4 nm @ 1 keV
Beam current range	5 pA - 20 nA	
Beam energy	100 ev - 30 keV	
Current stability	< 1.2 % in 11 h	max. 0.5 % / h
Min. feature size	18.2 nm line	20 nm
Min. grating periodicity	73 nm (32.4 nm line)	100 nm (50 nm line)
Stitching accuracy (100 μm write field, 10 keV)	mean $+3\sigma = 36$ nm	mean $+3\sigma < 60$ nm
Overlay accuracy	mean $+3\sigma = 39$ nm	mean $+3\sigma < 40$ nm
z sensing reproducibility	0.74 μm	< 1 μm

Key Features

- TFE gun
- Cross over free beam path
- High beam current density
- Compound objective lens for lowest beam aberrations
- Digital controlled electron optics column

- Fast electrostatic beam blanking
- 45 mm laser interferometer stage
- True closed loop piezo control for finest sample position
- 2 nm XY position resolution at any WD, WF size and SEM magn
- WFs from 0.5 μm to 2mm with automated calibration and selection
- 10 MHz DSP controlled high speed
- pattern processor
- System control software
- Multi user interface
- SEM inspection software
- Image archiving software
- Dimensional metrology software
- Integrated GDSII editor
- Proximity effect correction
- Data post-processor

D UHV Evaporator

Ultra High Vacuum (UHV) evaporator supplied by Instrumentti Mattila; manufactured and installed 1998.
System includes:

- E-gun, Telemark TT 10
- Cryopump, Cryo-torr 8

- Ion Gun, Tectra IonEtch GenII

Materials evaporated: Au, Ag, Ti, Nb, Ta, Cu, Al, Bi, V, Ge, Pt, Sn, Pd, Mo, Si
6 materials can be in the chamber at a time.

E RIE/CVD

Oxford Instruments Plasmalab80Plus
Combined instrument for reactive ion etching (RIE), plasma etching (PE) or plasma enhanced chemical vapor deposition (PECVD)

Property	Value
Wafer size	Up to 7 x 2", 4 x 3", 2 x 4" or one 6" or 8"
Substrate temperature	-150 °C to +400 °C

Available gases: Ar, O_2, SF_6 ja CHF_3